Advances in Colloid and Interface Science 235 (2016) 214–232

Contents lists available at ScienceDirect

Advances in Colloid and Interface Science

journal homepage: www.elsevier.com/locate/cis

Historical perspective

The hydrodynamics of bubble rise and impact with solid surfaces

Rogerio Manica [a], Evert Klaseboer [a], Derek Y.C. Chan [b,c,*]

[a] Institute of High Performance Computing, 1 Fusionopolis Way, 138632, Singapore
[b] Department of Mathematics & Statistics, The University of Melbourne, Parkville, 3010, Australia
[c] Department of Chemistry and Biotechnology, Swinburne University of Technology, Hawthorn, 3122, Australia

ARTICLE INFO

Available online 25 June 2016

Keywords:
Young–Laplace equation
Terminal velocity
Thin film drainage
Mobile–immobile interfaces
Bubble deformation
Bubble surface interaction

ABSTRACT

A bubble smaller than 1 mm in radius rises along a straight path in water and attains a constant speed due to the balance between buoyancy and drag force. Depending on the purity of the system, within the two extreme limits of tangentially immobile or mobile boundary conditions at the air–water interface considerably different terminal speeds are possible. When such a bubble impacts on a horizontal solid surface and bounces, interesting physics can be observed. We study this physical phenomenon in terms of forces, which can be of colloidal, inertial, elastic, surface tension and viscous origins. Recent advances in high-speed photography allow for the observation of phenomena on the millisecond scale. Simultaneous use of such cameras to visualize both rise/deformation and the dynamics of the thin film drainage through interferometry are now possible. These experiments confirm that the drainage process obeys lubrication theory for the spectrum of micrometre to millimetre-sized bubbles that are covered in this review. We aim to bridge the colloidal perspective at low Reynolds numbers where surface forces are important to high Reynolds number fluid dynamics where the effect of the surrounding flow becomes important. A model that combines a force balance with lubrication theory allows for the quantitative comparison with experimental data under different conditions without any fitting parameter.

Contents

* Corresponding author at: Department of Mathematics & Statistics, The University of Melbourne, Parkville, 3010, Australia. Tel.: +61 3 8344 5556; fax: +61 3 8344 4599.
E-mail address: D.Chan@unimelb.edu.au (D.Y.C. Chan).

http://dx.doi.org/10.1016/j.cis.2016.06.010
0001-8686/

1. Introduction

1.1. Background and motivation

Bubbles rising in water have probably fascinated mankind since the earliest of times. Leonardo da Vinci observed that large bubbles could follow a non-rectilinear path when rising under buoyancy [1,2]. But da Vinci was certainly not the only one to be intrigued by bubbles. For example, the inventor of the microscope, Anthoni van Leeuwenhoek [3], when describing an 'airpump' to study the presence of air in water and blood, states that "…een groote quantiteit lugt-bellen uijt het water op quamen, en als op borrelden, en nog meer, als ik een weijnig stootinge aan het glas quam te maken." ("a large quantity of bubbles came out of the water, rose, and even more, when I gently tapped on the glass").

Our knowledge of fluid dynamics improved over the next centuries. For example, the concept of surface tension was first introduced in 1805 by Young [4], who studied, without using equations, the shape of the fluid–fluid interface under capillary forces. In 1806 Laplace [5] used a force balance method in the normal and tangential direction to provide an equation of the fluid interface. Gauss [6] analysed this problem using the minimization of the interfacial area under the effect of interfacial tension.

Fluid flow in thin films was first analysed by Reynolds [7], resulting in the lubrication equations. In the 20th century, the use of coherent (or laser) light made it possible to measure the thickness of thin films. For example, Derjaguin and Kussakov [8] discovered the inverted curvature (a so-called dimple) of a bubble pressed against a surface using interferometry. In the 21st century, again advances in optics are improving our understanding in this area; this time it is the accessibility of high-speed cameras that drives progress [9,10]. Features that were too fast for the human eye to capture, can now be explored and examined with hundreds of thousands of frames per second, revealing a wealth of interesting physics.

Single bubbles rising in an infinite medium have been studied extensively, although major issues, such as the tangential mobility of the surface are still not fully understood. Bubbles interacting with other bubbles or surfaces have received much less attention [11]. Perhaps the simplest case is the interaction of a rising bubble with a horizontal solid surface, which is the focus of the current article. The understanding of this phenomenon requires knowledge of the bubble–wall interaction, for example the dynamics of the thin water film that forms between the bubble and the surface. In this work, we will mainly study air bubbles in water, which are of most practical importance for industrial and environmental applications. With that in mind, it now seems timely to write a review with the progress made so far for bubble rise and interaction with surfaces considering theoretical modelling of high quality experimental data.

1.2. Perspective

In this review we focus on the theoretical modelling of very reliable experimental data on the combined effects of bubble rise and impact with horizontal solid surfaces. Bubble rise has been studied extensively due to the appearance of intriguing features depending on the size of the bubble. Smaller bubbles with radius $R < 50$ μm for air bubbles in water tend to rise under Stokes flow conditions and the bubble velocity for an ultra clean system (mobile interface) is known analytically [12,13]. This result was confirmed experimentally [14,15] with extensive purging of the system to eliminate any residual impurity. However, it has been observed that exposure of the ultra-clean water to the atmosphere is enough to contaminate the sample [14] and the bubble will then rise with tangentially immobile boundary condition, in agreement with Stokes' law for a rigid sphere [16].

Bubbles of intermediate sizes ($50 < R < 1000$ μm for air bubbles in water) rise in a straight path and the problem is axisymmetric, which facilitates theoretical analysis, but results are mostly empirical [17]. Bubbles of even larger size rise in a spiral or a zig-zag path [18–22]. Bubbles in aqueous sugar solutions attain complicated shapes and rising behaviour [23].

Considerable effort has been devoted to investigate the variation of the terminal speed of bubbles with concentrations of different surfactants [24,25]. It was proposed that small concentrations of surfactant generate a surface tension gradient and the boundary condition at the top of the rising bubble is different from that at the rear [26,27] resulting in a so-called spherical cap model. Theoretical work was performed to explain the experimental observations [28–30] as well as numerical simulations [31,32]. For the case of Stokes flow an analytical solution for the spherical cap model was obtained [33].

Bubbles interacting with various surfaces have also received attention. For Stokes flow, analytical results are known for different systems including tangentially immobile [34] and mobile boundary conditions [35] at the bubble surface. Experiments were also performed for such bubbles rising against surfaces [36–38], which confirmed the theoretical results.

The interaction between bubbles (rising under buoyancy) and surfaces at relatively high Reynolds numbers is an active area of research until this day. Early experiments on bouncing bubbles mainly investigated side view images [39–47] while no information about the thin film drainage was collected. On the other hand, experiments capturing thin film drainage using interferometry were done at low frame rates [8,48–50]. Unfortunately a high frame rate is required to capture the fast changing film on the microscale. It is only recently that the use of synchronized high-speed cameras allowed for both observations simultaneously [9,10,51].

This review is organized in the following format. In Section 2 we investigate bubbles rising in a liquid and impacting with surfaces for small Reynolds numbers (Stokes flow). These are generally small bubbles ($R < 50$ μm) where surface forces are important during interaction with the surface. In Section 3 we look at bubbles rising in a liquid and interacting with surfaces for large Reynolds numbers where deformation during rise also becomes important. These are intermediate size bubbles (50 μm < R < 1 mm) where fluid dynamics aspects of the problem become more important. In Section 4 we provide a discussion on various aspects of bubble rise and impact such as the first appearance of a dimple and peculiar experiments with mobile film drainage and immobile rise behaviour. In Section 5 conclusions are presented.

1.3. Scope

In industrial multiphase reactors it is often necessary to predict areas where coalescence or adhesion can occur and knowledge of bubble–wall interaction is a prerequisite for a better design of such equipment. Another application area is in the augmentation of heat transfer due to impacting bubbles on a surface [52].

In Fig. 1 we show a photograph and a schematic of an air bubble with radius R and surface tension σ rising under buoyancy with terminal velocity $V = V_T$ in a medium with density ρ and viscosity μ.

We assume that the continuous phase is a Newtonian fluid, so that the rise of the bubble and impact with a surface can be modelled by the Navier–Stokes and continuity equations written as [53]

$$\rho\left(\frac{\partial \mathbf{u}}{\partial t} + \mathbf{u}\cdot\nabla\mathbf{u}\right) = -\nabla p + \mu\nabla^2\mathbf{u} - \rho g\mathbf{k} \tag{1}$$

$$\nabla\cdot\mathbf{u} = 0 \tag{2}$$

where $\mathbf{u}$ is the velocity vector and p the pressure.

After scaling the dimensional coordinates in Eq. (1) with the bubble diameter and velocities with the bubble velocity, the Reynolds number, the ratio of typical magnitudes of inertia terms to viscous terms, emerges

$$Re = \frac{2R\rho V}{\mu} \tag{3}$$

A Reynolds number smaller than unity indicates the system behaves as Stokes flow (i.e. viscosity dominated) while for large Reynolds numbers, the system is under potential flow conditions (i.e. inertia dominated). Note that here the Reynolds number refers to the terminal velocity $V = V_T$, but later in the article it can also apply to the instantaneous velocity.

The internal pressure (Laplace pressure) of a bubble is equal to the surface tension σ times the curvature ($=2/R$ for a spherical bubble). If the inertial pressure $\rho V^2/2$ becomes larger than the Laplace pressure, surface tension will no longer be able to sustain the spherical bubble shape. The Weber number expresses the ratio of these two effects as

$$We = \frac{2R\rho V^2}{\sigma} \tag{4}$$

A Weber number smaller than one indicates a spherical bubble, while for Weber numbers larger than one but smaller than ~3, an ellipsoidal bubble shape can be expected. The ellipse is directed with its longest axis perpendicular to the flow. The inertial pressure pushes at the top and bottom of the bubble and creates a lower pressure at the sides, due to larger velocities.

Numerical simulations using an axisymmetric boundary-fitted coordinate formulation [54,55] and a full three-dimensional solution of the Navier–Stokes equations for unsteady rising bubbles that take into account deformation in a self-consistent way are complex to implement and demanding in terms of computational resources [56]. Moreover, very fine grids are needed to capture details of the film drainage, which occurs at length scale orders of magnitude smaller than the bubble size. Nonetheless recent computational progress allowed numerical simulations of bubble impact with a surface and bounces were captured using for example the numerical code Gerris.

Instead of solving the full equations using grid based numerical simulations, simplifications to the Navier–Stokes equations that are valid in different experimental regimes based on the Reynolds and Weber numbers can be made.

We will consider bubbles with mobile and tangentially immobile boundary conditions represented in Fig. 2.

1.4. Balance of forces

When discussing the analytically calculated force on a bubble as compared to detailed numerical simulations, Magnaudet & Eames [18] state that this is “a potentially powerful tool”. The balance of forces implicitly assumes that these forces can be added.

In this section we describe a balance of forces approach that can be used for bubbles in both Stokes flow and high Reynolds number flow from the moment it starts its movement from rest, reaches terminal velocity and impacts with a surface. The forces to be considered are: buoyancy, drag, added mass, history, film, Van der Waals and electrical

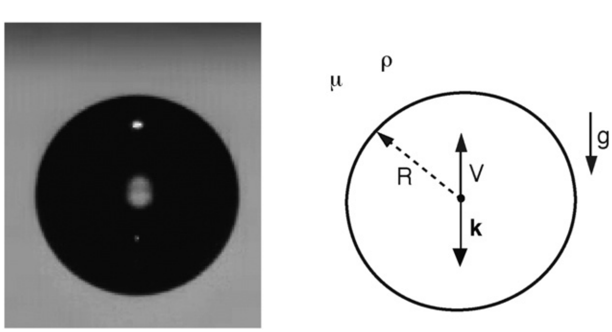

Fig. 1. Photograph of a spherical bubble rising in water together with the schematic of a bubble rising in bulk where the following parameters are defined: bubble radius R, bubble velocity (of the centre of mass) V, density ρ and viscosity μ of the surrounding liquid. Gravity g is pointing downward in the unit vector $\mathbf{k}$ direction.

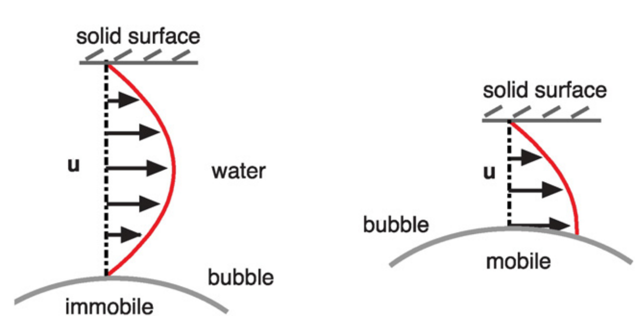

Fig. 2. Schematic of a bubble with mobile and tangentially immobile boundary conditions. For the immobile boundary condition, the tangential velocities at both the surface–water and air–water interfaces are zero. In the mobile boundary condition case, the shear stress at the air–water interface is zero.

double layer. There is also a distinction depending on the boundary conditions at the bubble surface. In a clean system the boundary is mobile (zero stress) while in a system containing surfactants ('dirty') the boundary becomes tangentially immobile. The sum of forces on the bubble (Newton's second law) is given by

$$\sum \mathbf{F} = \mathbf{F}_B + \mathbf{F}_D + \mathbf{F}_A + \mathbf{F}_H + \mathbf{F}_F + \mathbf{F}_{VDW} + \mathbf{F}_{EDL} = m\mathbf{a} \approx 0 \tag{5}$$

The mass of the bubble itself, m, is virtually zero, hence the appearance of the term '0' on the right hand side. Note that the acceleration vector $\mathbf{a} = dV/dt\,\mathbf{k}$ is non-zero. In this equation $\mathbf{F}_A$ is the added mass force, $\mathbf{F}_B$ is the buoyancy force, $\mathbf{F}_D$ is the drag force, $\mathbf{F}_H$ is the history force, $\mathbf{F}_F$ is the film force, $\mathbf{F}_{VDW}$ is the Van der Waals force and $\mathbf{F}_{EDL}$ is the electrical double layer force. Each term in Eq. (5) can be written in terms of the fluid properties such as μ and ρ, the radius of the bubble R, the velocity of the bubble V and the acceleration of the bubble dV/dt. In the next sections we will describe all the forces individually taking into account the forces that are relevant for the particular system investigated.

2. Spherical bubbles in Stokes flow

2.1. Forces in Stokes flow in bulk

In this section we will study small bubbles in Stokes flow, which are relevant in colloid science. If the bubble is small ($R < 50$ μm) the Reynolds number (Eq. (3)) is smaller than unity, inertial effects are negligible and the system can be treated with Stokes flow theory. Under this assumption Eq. (1) becomes

$$\rho\frac{\partial \mathbf{u}}{\partial t} = -\nabla p + \mu\nabla^2\mathbf{u} - \rho g\mathbf{k} \tag{6}$$

By solving Eqs. (2) and (6) analytically for the fluid velocity for a bubble rising in a liquid and then calculating the different contributions of the total force on the bubble, the trajectory of the bubble can be obtained from a balance of forces. In the following we discuss these forces in detail. If the Weber number (Eq. (4)) is also small, the bubble remains spherical.

In bulk the surface forces and film forces are not important and the only forces that remain in Eq. (5) are buoyancy, drag, added mass and history. The equation of motion of the bubble [17] becomes

$$\underbrace{\frac{4}{3}\pi R^3 \rho C_m \frac{dV}{dt}}_{\text{added mass}} = \underbrace{\frac{4}{3}\pi R^3 \rho g}_{\text{buoyancy}} - \underbrace{6\pi\mu R V \lambda}_{\text{drag}} - \underbrace{6\pi\mu R \int_0^t G(t-\tau)\frac{dV}{d\tau}d\tau}_{\text{history}} \tag{7}$$

where the added mass coefficient $C_m = 1/2$ and $\lambda = 1$ or $2/3$ depending whether the boundary condition on the bubble surface is immobile or mobile. Eq. (7) is a general equation for bubbles in Stokes flow rising in a liquid. We will look at each force individually in the next subsections.

2.1.1. Buoyancy force

A bubble rising in a liquid experiences a buoyancy force, which is equal to the density of the fluid ρ, multiplied by the acceleration due to gravity g, and the volume of the bubble:

$$\mathbf{F}_B = -\rho g \frac{4}{3}\pi R^3\ \mathbf{k} \tag{8}$$

(note that the density of the gas has been neglected when compared to that of the liquid). A minus sign appears since $\mathbf{k}$ is defined to point downwards (see Fig. 1).

2.1.2. Drag force

The drag force can be written as

$$\mathbf{F}_D = \begin{cases} 6\pi\mu R V\ \mathbf{k} & \text{(tangentially immobile)} \\ 4\pi\mu R V\ \mathbf{k} & \text{(mobile)} \end{cases} \tag{9}$$

The immobile result (like a solid sphere) corresponds to the Stokes law for spheres in a liquid while the mobile result is valid for bubbles with zero tangential stress. In most practical situations surfactants and impurities in the water will render bubbles to behave like solid spheres with immobile boundary condition.

2.1.3. Added mass force

If the bubble is accelerating some surrounding fluid must also accelerate (hence the name "added mass"). In the Navier–Stokes equations (Eq. (1)), the added mass force originates from the unsteady term $\rho\partial\mathbf{u}/\partial t$ and is given by:

$$\mathbf{F}_A = \rho\frac{4}{3}\pi R^3 C_m \frac{dV}{dt}\ \mathbf{k} \tag{10}$$

The added mass force appears in both (unsteady) Stokes and high Reynolds number flows. For a spherical bubble far away from any other objects, the added mass coefficient is $C_m = 1/2$ for both cases. The added mass force is of purely inertial origin. There is another force that depends on the acceleration of the bubble, the history force.

2.1.4. History force

Another force that is of viscous origin is the history force, also known as the Basset force [57,58]. This force is "originating from the unsteady diffusion of vorticity around the bubble" [18] or in other words, the drag force needs some time to establish itself resulting in the history force (hence the appearance of the viscosity in this force)

$$\mathbf{F}_H = 6\pi\mu R \int_0^t G(t-\tau)\frac{dV}{d\tau}d\tau\ \mathbf{k} \tag{11}$$

where the kernel function G depends on whether the boundary condition at the surface of the bubble is mobile or tangentially immobile [59]

$$G(t-\tau) = \begin{cases} \dfrac{3}{\sqrt{\pi}}\xi^{-1} & \text{(a, tangentially immobile)} \\ \dfrac{4}{3}e^{\xi^2}\,erfc(\xi) & \text{(b, mobile)} \end{cases} \tag{12}$$

with $\xi = \sqrt{\dfrac{9\mu(t-\tau)}{R^2\rho}}$ and $erfc(\xi) = \dfrac{2}{\sqrt{\pi}}\int_\xi^\infty exp(-s^2)ds$.

The expressions in Eq. (12) are only valid for low Reynolds flows. Since the past acceleration $dV/d\tau$ appears in Eq. (11), it is also known as the "history force" or Basset memory integral. Note that the immobile G shows a $(t-\tau)^{-1/2}$ singularity under the integral sign. However the mobile expression for G remains finite at $t-\tau = 0$. The above expression can be obtained by solving the Stokes equations (Eq. (5)) and using a Fourier transform [60]. In Fig. 3, we compare the function G for mobile and immobile interfaces.

A closed form expression for the history force can no longer be obtained for a bubble approaching a wall. Nevertheless we use Eq. (12) as a first approximation.

Even though approximate results have been proposed for the history force [61], due care must be taken to calculate the history force properly.

2.2. Terminal velocity

A bubble rising at a sufficiently large distance away from any boundaries in a quiescent liquid will attain a constant velocity, known as terminal velocity V_T. When the velocity is constant the drag (Eq. (9)) and

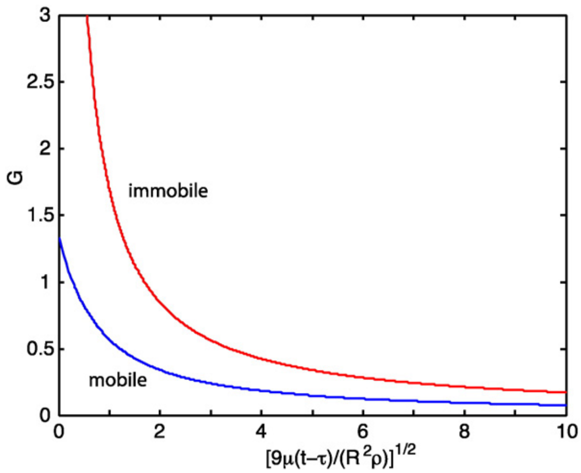

Fig. 3. The kernel function G (Eq. (12)) for mobile and immobile boundary conditions as a function of the square root of time. Note that the mobile curve remains finite at the origin of time.

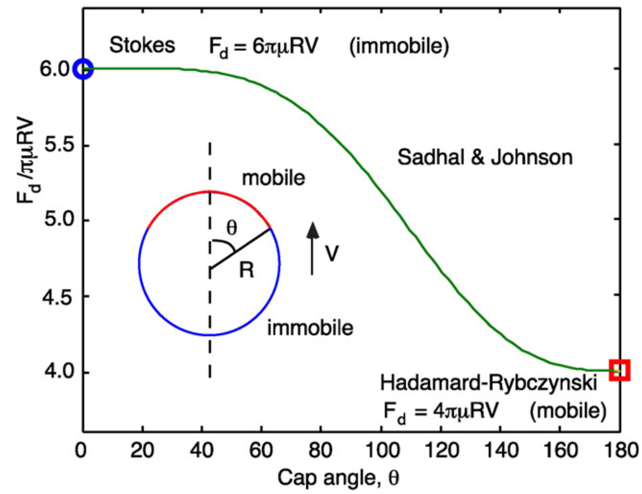

Fig. 4. Analytical solution of the drag force for a spherical bubble rising with speed $V = V_T$ upwards under the spherical cap model assumption (due to Sadhal and Johnson [33], continuous line). The angle θ indicates the region for which the surface is 'clean' (i.e. zero stress, red section), while the remainder of the bubble (blue section) is considered tangentially immobile. The Stokes as well as Hadamard–Rybczynski drags are the two limiting cases for fully immobile (blue circle) and mobile (red square) bubbles and correspond to $\theta = 0$ and ($\theta = \pi$).

buoyancy (Eq. (8)) forces are the only two forces acting on the bubble, and the vectorial sum of these two forces must be zero. For bubbles with tangentially immobile or mobile interfaces, from Eqs. (8) and (9), the terminal velocity is

$$V_T = \begin{cases} \dfrac{2\rho g R^2}{9\mu} = V_S & (\text{a, tangentially immobile}) \\ \dfrac{\rho g R^2}{3\mu} & (\text{b, mobile}) \end{cases} \tag{13}$$

Thus for a bubble with mobile boundary, the terminal velocity is larger by a factor 3/2 compared to the tangentially immobile case.

In general, besides the two limits of completely mobile or immobile, bubbles can also exhibit partially mobile behaviour. This is often termed "spherical cap bubble". An analytical solution for the spherical cap model that presumes that the surface is free of surfactant at the top, gives rise to a mobile boundary condition (zero tangential stress). The bottom surface is completely covered with surfactants, resulting in a tangentially immobile boundary condition (zero tangential velocity). A schematic of such a spherical cap bubble is shown in the inset of Fig. 4. The drag force $\mathbf{F}_D$ experienced on such a spherical cap bubble was calculated analytically by Sadhal & Johnson [33] and they found (note that the viscosity of the bubble has been neglected here):

$$\mathbf{F}_D = 6\pi\mu VR\left\{1 - \frac{2\theta - \sin\theta - \sin 2\theta + \frac{1}{3}\sin 3\theta}{6\pi}\right\}\mathbf{k} \tag{14}$$

where $\mathbf{F}_D$ depends on the cap angle θ defined in Fig. 4. For the case of a bubble covered with surfactants the boundary condition is immobile ($\theta = 0$) and the drag obeys the classical Stokes law [16] $\mathbf{F}_D = 6\pi\mu VR$. On the other hand, for a fully mobile bubble ($\theta = \pi$), the boundary condition is zero stress and the drag obeys the theoretical Hadamard–Rybczynski [12,13] result $\mathbf{F}_D = 4\pi\mu VR$. The analytical result of Eq. (14) as well as limiting cases are shown in Fig. 4.

Comparisons of terminal velocities from Eq. (13) with experiments [14,15] are shown in Fig. 5. To achieve the terminal velocity corresponding to the Hadamard–Rybczynski formula (mobile velocity of Eq. (13)) it was required to clean the water system for several hours before taking the measurements.

The inset of Fig. 5 shows what happens over time when bubbles of radius $R = 40$ μm rise in a liquid [14]. Initially at time $t = 0$ the bubbles rise with terminal velocity in agreement with Stokes' law ($V_T = 3.5$ mm/s according to Eq. (13), dashed line at the bottom). After purging for 3 h the bubbles rise under mobile boundary condition ($V_T = 5.2$ mm/s). If the system is kept sealed, the terminal velocity remained the same. But if the container was opened to the atmosphere for a few hours, the terminal velocity decreases and tends towards the Stokes law for solid spheres once more. Intermediate velocities probably correspond to bubbles that are partially covered with surfactants (spherical cap bubbles).

It thus turns out that experiments that were able to observe bubbles with mobile boundary condition in Stokes flow required extensive cleaning. In general small bubbles in industrial applications will most likely have immobile interfaces, when no extreme care has been taken concerning the cleanliness of the system.

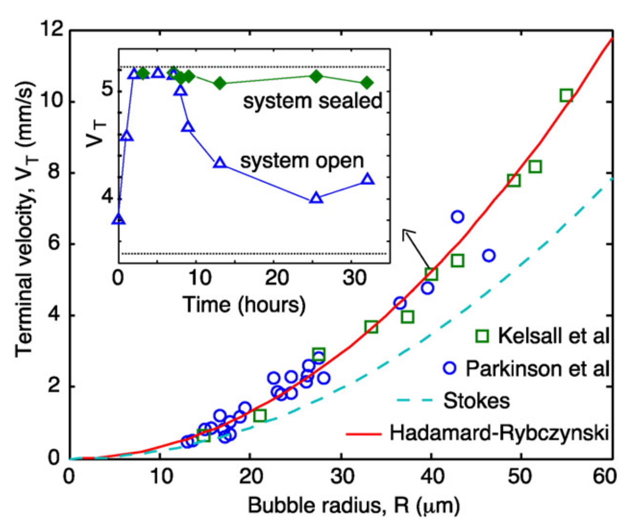

Fig. 5. Terminal velocities for bubbles in water under Stokes flow. Comparison between experiment for air bubbles by Parkinson et al. [15] and O_2 bubbles of Kelsall et al. [14] with the Hadamard–Rybczynski result (Eq. (13)b). The Stokes law (Eq. (13)a) is also plotted. Inset shows the effect of purging and opening the container to the atmosphere on the terminal velocity for O_2 bubbles with radius about 40 μm in 10^{-4} M aqueous $NaClO_4$ solution at temperature 298 K.

2.3. Bubble rising from rest in bulk

We continue with Eq. (7) to investigate the relative importance of each force for a bubble starting from rest before approaching its terminal speed in an unbounded initially quiescent liquid. The terminal velocity of the immobile bubble (Eq. (13)) is used as a velocity scale V_S (Eq. (13)a). Note that we use the same velocity scale for the mobile and immobile cases. By choosing the following time scale

$$t_S = \frac{V_S}{2g} = \frac{\rho R^2}{9\mu} \tag{15}$$

Eq. (7) can be written with no parameters at all ($t = t_S t^*$; $V = V_S V^*$, $\tau = t_S \tau^*$, $C_m = 1/2$).

$$\frac{dV^*}{dt^*} = 1 - \lambda V^* - \int_0^{t^*} G \frac{dV^*}{d\tau^*} d\tau^* \tag{16}$$

where $\lambda = 1$ for immobile and $\lambda = 2/3$ for mobile bubble surfaces and

$$G = \begin{cases} \dfrac{3}{\sqrt{\pi(t^* - \tau^*)}} & \text{(a, immobile)} \\ \dfrac{4}{3} e^{t^* - \tau^*} erfc\left(\sqrt{t^* - \tau^*}\right) & \text{(b, mobile)} \end{cases} \tag{17}$$

The analytical solution of Eq. (16) for the immobile boundary condition ($\lambda = 1$) is given by Clift, Grace and Weber [17] on page 289, with initial condition $V^* = 0$ at $t^* = 0$.

$$V^* = 1 - \left(\frac{\alpha}{\alpha - \beta}\right) exp\left(\beta^2 t^*\right) erfc\left(\beta\sqrt{t^*}\right) - \left(\frac{\beta}{\beta - \alpha}\right) exp\left(\alpha^2 t^*\right) erfc\left(\alpha\sqrt{t^*}\right) \tag{18}$$

where $\alpha = \frac{3}{2}\left[1 + \sqrt{1 - 4/9}\right]$ and $\beta = \frac{3}{2}\left[1 - \sqrt{1 - 4/9}\right]$.

If the history force is neglected, with initial condition $V = 0$ at $t = 0$ (bubble at rest), the solution of Eq. (7) for the velocity of the bubble, V, as a function of time is given analytically by

$$V(t) = \frac{2\rho g R^2}{9\mu} \begin{cases} 1 - exp\left(-9\mu t/\left(\rho R^2\right)\right) & \text{(a, immobile)} \\ \dfrac{3}{2}\left[1 - exp\left(-6\mu t/\left(\rho R^2\right)\right)\right] & \text{(b, mobile)} \end{cases} \tag{19}$$

In Fig. 6, we compare the results of the numerical solution of Eq. (16) combined with Eq. (17)b for the mobile bubble, the analytical solutions of Eq. (18) for the tangentially immobile bubble with history force included and omitting the history force Eq. (19) for both mobile and immobile.

The distance S travelled by the bubble starting from rest can be calculated by integrating V with respect to time and is given in Fig. 6b, where the scale for S is $V_S^2/(2g)$. The acceleration of the bubble can be obtained by differentiating Eq. (19) with respect to time

$$\frac{dV}{dt} = 2g \begin{cases} exp\left(-9\mu t/\left(\rho R^2\right)\right) & \text{(a, immobile)} \\ exp\left(-6\mu t/\left(\rho R^2\right)\right) & \text{(b, mobile)} \end{cases} \tag{20}$$

Note that the initial acceleration of the bubble is $2g$ due to the added mass coefficient being $C_m = 1/2$.

Thus history force and added mass are both important for bubbles rising from rest. In the next section we will analyse the behaviour of the balance of forces when a bubble impacts on a surface.

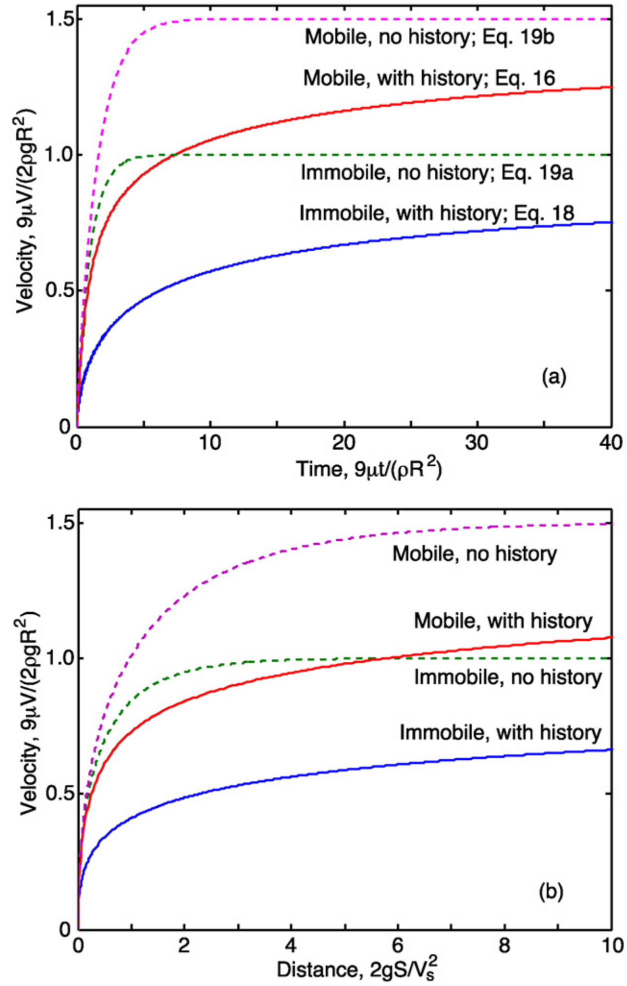

Fig. 6. Comparison of the bubble velocity rising from rest with and without history force as a function of (a) time and (b) distance.

2.4. Bubbles impacting on surfaces

In Section 2.2 we reviewed the terminal velocity that a bubble obtains if it is far away from any surface. In this section we will investigate what happens if it approaches a horizontal flat surface with terminal velocity (Fig. 7). In this context, the term 'terminal' is actually badly chosen, since the real terminal velocity will be zero. Therefore, we will use the more appropriate term 'approach velocity' instead of 'terminal velocity' to avoid confusion. The first case we will investigate is a small bubble approaching a surface under buoyancy. This example is particularly interesting from both a colloid/interfacial science and a fluid dynamics point of view. Effects from both fields of science occur, but are important at different times. It will connect the fluid dynamic forces with the more familiar colloidal interactions. Fluid dynamic forces dominate the process in the early approach stage, while colloidal forces become progressively more important towards the end of the settling process. The theory for this case is relatively straightforward, since inertial effects are largely absent, and it is possible to obtain analytical results for some limiting cases. This in turn will be useful in understanding the physics involved.

In the balance of forces of Eq. (5) we neglect surface forces for the moment and assume that $\mathbf{F}_B$, $\mathbf{F}_A$, and $\mathbf{F}_H$ are defined in Eqs. (8), (10) and (11) respectively. We also assume that $C_m = 1/2$ and that the history force remains the same as in bulk even though they are slightly modified due to presence of the wall. The resulting equation is identical to

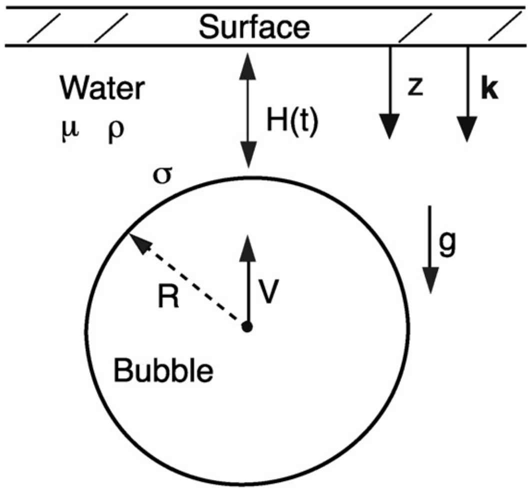

Fig. 7. Schematic of a bubble rising in bulk before hitting a flat horizontal surface. The main theoretical parameters are defined.

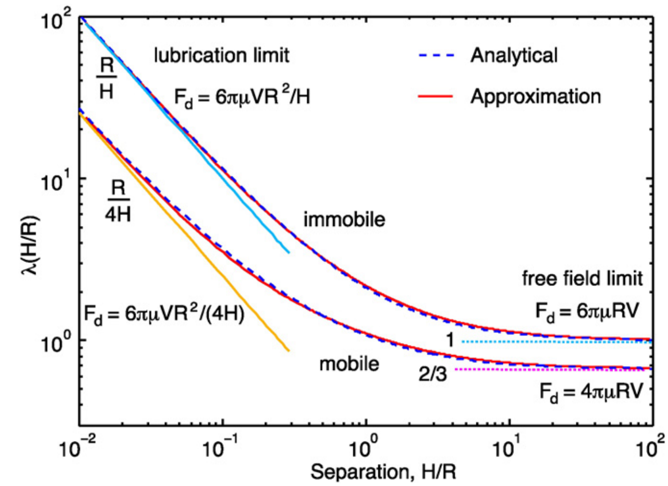

Fig. 8. The function λ of Eq. (22) for a spherical bubble in Stokes flow approaching a surface (solid lines) and according to the theories of Bart [35] and Brenner [34] (dashed lines). Around $H/R = 0.5$, the influence of lubrication and 'free-field' drags are equal. However, even for $H/R = 10$, the bubble already clearly 'feels' the wall.

Eq. (7) except that the drag force now also depends on the separation H between the top of the bubble and the surface (in Eq. (7) it only depended on the bubble surface mobility condition). For convenience, the drag force $\mathbf{F}_D$ is written in terms of a dimensionless function λ as

$$\mathbf{F}_D = 6\pi\mu RV\lambda\ \mathbf{k} \tag{21}$$

The exact analytical expression for λ involves infinite sums of hyperbolic functions [34,35]. Empirical approximations that are easier to use (maximum 1.3% error for all values of H/R) were given in Manica et al. [37]. Here we use approximated solutions of the form

$$\lambda = \begin{cases} 1 + \dfrac{R}{H} + \dfrac{3}{8}\dfrac{R}{(R+H)} & \text{(a, immobile)} \\ \dfrac{2}{3} + \dfrac{R}{4H} + \dfrac{3}{8}\dfrac{R}{(R+H)} & \text{(b, mobile)} \end{cases} \tag{22}$$

Eq. (22) reflects the summation of three effects. For the immobile case, the factor "1" represents the usual bulk drag force. The term with R/H represents the lubrication limit result. A third term is added which represents the fact that the bubble "sees" its own image. If the bubble is relatively far from the wall, this contribution is essentially a Stokeslet. This image Stokeslet will, when higher order terms are neglected, create a velocity $3V/(4r^*)$, at the location of the centre of the original bubble with $r^* = 2(R + H) / R$. Thus the bubble effectively feels an additional last term of Eq. (22) for both the immobile and mobile case. For the mobile bubble, the factor 2/3 represents the bulk drag, while the factor $R/(4H)$ represents the classical lubrication limit. When compared to the exact analytical solutions of Bart and Brenner, the maximum relative error is 3.4% for the immobile bubble and 5.2% for the mobile case.

In Fig. 8 we compare the value of λ for the approximation given by Eq. (22) (solid lines) with the analytical (dashed lines) for the mobile and immobile boundary conditions. Classical limiting forms are also indicated.

Unlike the bubble rising from rest, the solution cannot be written in a universal form. By solving Eq. (7) numerically considering λ from Eq. (22), the effect of history and added mass are not so pronounced (see Fig. 9). Neglecting these two forces, Eq. (7) can be simplified to (note that $V = -dH/dt$)

$$6\pi\mu R\lambda\frac{dH}{dt} = -\frac{4}{3}\pi R^3\rho g \tag{23}$$

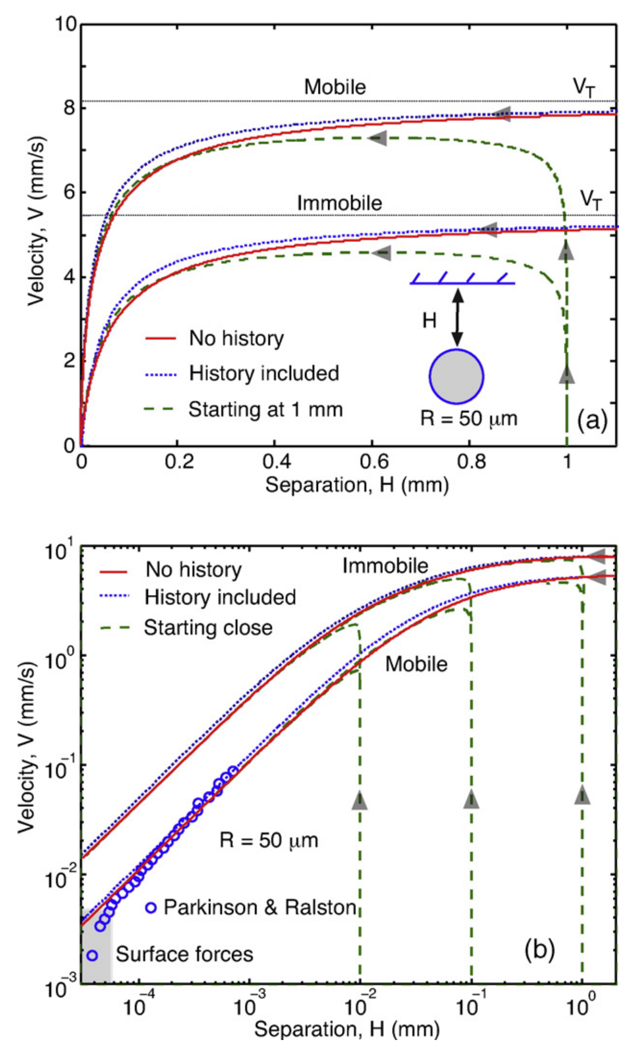

Fig. 9. The velocity of a bubble as it rises and interacts with a surface. (a) Velocity of the bubble ($R = 50$ μm) starting from infinity and at 1 mm for mobile and immobile boundary conditions. The dotted lines are the terminal velocities for the respective cases. (b) Similar to (a) but using log–log scale. Results are shown starting at different initial separations and the experiments of Parkinson & Ralston [36] are also shown for comparison. The grey bar corresponds to the separation where surface forces become important ($H < 50$ nm).

Using Eq. (22) an analytical solution of Eq. (23) can be found by integration and is given by

$$-\frac{2\rho gR}{9\mu}(t-t_o)=\frac{H-H_0}{R}+\ln\left(\frac{H}{H_0}\right)+\frac{3}{8}\ln\left(\frac{H+R}{H_0+R}\right) \tag{24a}$$

for the immobile case and

$$-\frac{2\rho gR}{9\mu}(t-t_o)=\frac{2(H-H_0)}{3R}+\frac{1}{4}\ln\left(\frac{H}{H_0}\right)+\frac{3}{8}\ln\left(\frac{H+R}{H_0+R}\right) \tag{24b}$$

for the mobile case, where $H_0=H(t_0)$.

In Fig. 9a we show the numerical solution of Eq. (7) for mobile and immobile bubble surface boundary conditions for a bubble with radius 50 μm for bubbles starting at $H_0=1$ mm and infinity. The terminal velocity is indicated by the horizontal dotted line. The approximate solutions of Eq. (23) assuming λ of Eq. (22) for immobile and mobile surfaces are also shown. In Fig. 9b we show the numerical solution of Eq. (7) in a log–log plot at different starting points (1.0, 0.1 and 0.01 mm). The velocity increases fast, but not enough to attain terminal velocity before hitting the surface. At short separations the theoretical results are compared with experiments of Parkinson and Ralston [36] where good agreement is found.

The theoretical results presented in Fig. 9 do not include surface forces, which are important at close separations as indicated by the grey bar in Fig. 9b. In the next section surface forces will be investigated.

2.5. Inclusion of surface forces

When the bubble is very close to the surface, surface forces due to Van der Waals $\mathbf{F}_{VDW}$ and electrical double layer $\mathbf{F}_{EDL}$ interactions become important [37]. We write $\mathbf{F}_{VDW}=2\pi R_{eff}E_{VDW}\mathbf{k}$ and $\mathbf{F}_{EDL}=2\pi R_{eff}E_{EDL}\mathbf{k}$ where E_{VDW} and E_{EDL} are respectively, the Van der Waals and electrical double layer interaction energy per unit area between the bubble and surface [62,63]. They are related to the corresponding force via the Derjaguin approximation (i.e. the force between two spheres with radius R_1 and R_2 is equal to $2\pi R_{eff}E_{VDW}$, where $1/R_{eff}=1/R_1+1/R_2$, thus here $R_{eff}=R$, since the wall is flat) [64]. Note, that in the force balance of Eq. (5), the added mass and history forces are ignored since accelerations are very small.

2.5.1. Van der Waals force

The Van der Waals interaction free energy per unit area between two flat plates (neglecting electromagnetic retardation due to relativistic effects) has the form [63]

$$E_{VDW}=-\frac{A}{12\pi H^2} \tag{25}$$

where A is the Hamaker constant (absolute value typically ranging from 10^{-19} to 10^{-20} J). For the case under consideration the Hamaker constant is negative (repulsive) [63]. When Van der Waals forces become important, we are usually in the lubrication limit of the function λ (i.e. $\lambda=R/H$) Eq. (22).

2.5.2. Electrical double layer force

If the concentration of salt is low, the electrical double-layer interaction (E_{EDL}) cannot be neglected. The electrical double layer interaction free energy per unit area can be calculated from the superposition approach for $\kappa H>2$ as [63,65]

$$E_{EDL}=\frac{64n_o k_BT}{\kappa}\tanh\left(\frac{e\psi_b}{4k_BT}\right)\tanh\left(\frac{e\psi_s}{4k_BT}\right)e^{-\kappa H} \tag{26}$$

where n_o is the number concentration (number density of the ions in bulk solution = mol/m^3) of monovalent (1:1) electrolyte, k_B is Boltzmann's constant, T the absolute temperature, $1/\kappa$ the Debye length and e the elementary charge of a single electron, ψ_b is the surface potential on the bubble and ψ_s the surface potential on the solid plate. The use of Eq. (26) is justified if the equilibrium film thicknesses, H_{eq} is larger than the Debye length ($\kappa H_{eq}>1$). Furthermore in the superposition limit, we do not need to be concerned with whether the surfaces interact under constant surface potential or constant surface charge [63].

Typical repulsive curves for electrical double layer (solid lines for different concentrations) and Van der Waals (dashed line for a given Hamaker constant $A=-4\times10^{-20}$ J) [37] are presented in Fig. 10. The buoyancy forces for bubbles of different size are represented by horizontal dotted lines. When the surface force exceeds the buoyancy force the bubble stops approaching. For example a bubble with radius $R=40$ μm in 1 mM concentration stops at point marked "A" due to electrical double layer repulsion while a bubble of $R=10$ μm in high salt stops at the separation marked "B" in the plot due to Van der Waals repulsion. Intermediate regions will require both Van der Waals and electrical double layer forces.

Neglecting added mass and history, the force balance Eq. (5), is written with the aid of the Derjaguin approximation as [37]

$$6\pi\mu R\lambda\frac{dH}{dt}=-\frac{4}{3}\pi R^3\rho g-\frac{RA}{6H^2}+2\pi R\frac{64n_o k_BT}{\kappa}\tanh\left(\frac{e\psi_b}{4k_BT}\right)\tanh\left(\frac{e\psi_s}{4k_BT}\right)e^{-\kappa H} \tag{27}$$

In situations where the electrical double layer term can be neglected, Eq. (27) can be integrated analytically for immobile bubbles ($\lambda=R/H$) to give the separation as a function of time as

$$H(t)=\sqrt{\eta^2+\left(H_0^2-\eta^2\right)e^{-2t/\tau}} \tag{28}$$

where H_0 is the initial separation, $\eta^2=|A|/(8\pi\rho gR^2)$ and $\tau=9\mu/(2\rho gR)$. A similar result can be obtained for the fully mobile bubble in the limit $H/R\to0$.

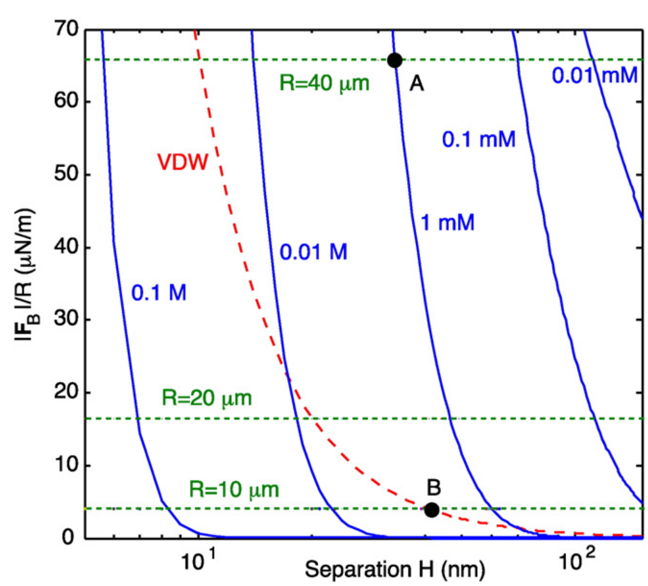

Fig. 10. Typical equilibrium interaction curves corresponding to Van der Waals (dashed red line) with $A=-4\times10^{-20}$ J and electrical double layer (solid blue curves) for different concentrations (with surface potential −45 mV and −60 mV) indicated in the curves. Increasing salt concentration decreases the electrostatic repulsion. Typical buoyancy forces for small bubbles ($R=10$, 20 and 40 μm) are represented by horizontal lines.

In Fig. 11, the numerical solutions of Eq. (27) are compared to experiments [36] of small bubbles rising under gravity against a titania surface in a solution at pH 6.3 under different concentrations of the electrolyte $N(CH_3)_4Br$. Details of the experiment as well as the theory can be found in Manica et al. [37]. The separation was obtained with interference fringes (see also Section 3.3). The interaction force is repulsive so that the bubble will never touch the surface but instead settles close to the surface at the separation where the surface force balances the buoyancy force. The final separation of cases (a) and (b) is dominated by a repulsive electrical double layer while for cases (c) and (d) by the Van der Waals force, which is also repulsive for the system investigated.

The agreement between experiment and theory is impressive, especially when one considers that there are no fitting parameters in the theory. The approach velocity was $V_T = 0.079$ cm/s for $R = 19$ μm and $V_T = 0.54$ cm/s for $R = 50$ μm. The Reynolds number (Eq. (3)) based on this approach velocity ranges from Re $= 0.03$ to 0.54 and the Weber number (Eq. (4)) from $We = 3.2 \times 10^{-7}$ to $We = 4.0 \times 10^{-5}$ for the $R = 19$ μm and $R = 50$ μm bubbles respectively. These values indicate that the whole process including approach is under the Stokes flow regime (Re < 1) and that the deformation of the bubbles is truly negligible ($We \ll 1$). In the next section we will investigate bubbles that are approaching under significantly higher Reynolds numbers and exhibit deformation.

3. Deformable bubbles with high Reynolds number

In this section we cover large bubbles ($0.1 < R < 1$ mm) rising and impacting on solid surfaces at large Reynolds numbers up to 700. The balance of forces is very similar to the one presented for the previous section but the terms become more complex due to deformation of the bubble and inertial effects. Due to the larger bubble size, buoyancy will be larger, resulting in larger approach velocities. At such large speeds the bubble deforms considerably during impact with the surface. If the We number (Eq. (4)) is larger than unity, deformation of the bubble is also important during rise and the bubble no longer remains spherical but instead assumes an ellipsoidal shape.

In Fig. 12a we introduce the parameters that are needed for the development of the theoretical model. Depending on size and velocity $V(t)$, the bubble can attain an approximate oblate ellipsoid shape during rise as indicated by the dashed shape. We define the horizontal radius R_H and the vertical radius R_V as the bubble rises in bulk before impacting

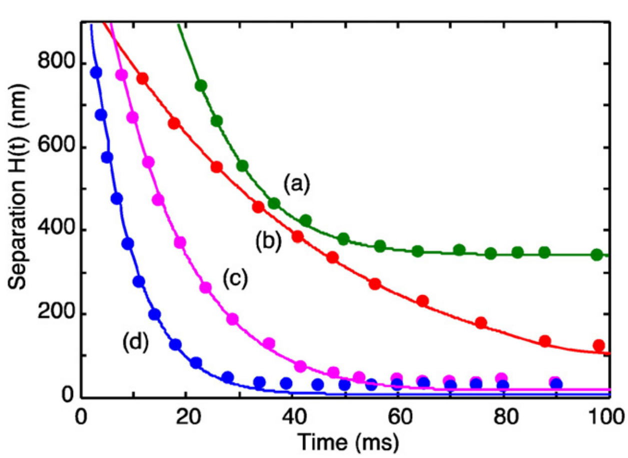

Fig. 11. Air bubble approaching a titania surface. Comparison between theory and experiment for (a) $R = 19$ μm, no salt added (b) $R = 10$ μm; 1 mM $N(CH_3)_4Br$ (c) $R = 27$ μm; 10 mM $N(CH_3)_4Br$ (d) $R = 50$ μm; 100 mM $N(CH_3)_4Br$. Experimental data correspond to the circular symbols while the theory is given by solid lines. The equilibrium heights H_{eq} correspond to 340 nm, 100 nm, 20 nm and 10 nm for cases (a) to (d) respectively. For all cases the pH = 6.3, A $= -4 \times 10^{-20}$ J (repulsive). The surface potentials are $\Psi_1 = -60$ mV (bubble) and $\Psi_2 + = -45$ mV (titania).

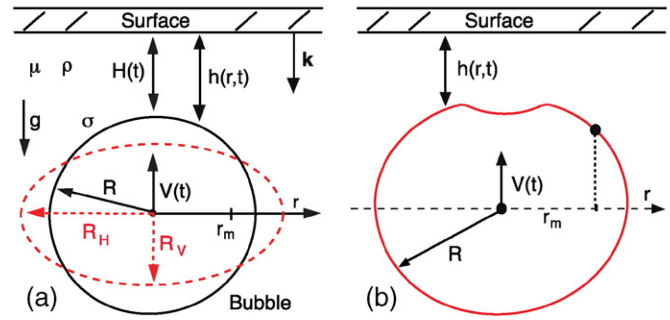

Fig. 12. Schematic of bubbles rising and impacting a solid surface. There are two sources of deformation: (a) Deformation in bulk (b) deformation during impact with the surface. In reality the ratio of dimple height to film width is very small. Theoretical variables including the length of the computational domain r_m are defined.

a surface. The equivalent radius R based on the volume of the bubble is defined as

$$R = \left(R_V R_H^2\right)^{1/3} \tag{29}$$

and the aspect ratio of the deformed bubble is defined as $\chi = R_H/R_V$. When the bubble impacts the surface, the top also deforms due to lubrication effects (see Fig. 12b).

It is important to consider both deformations in a self-consistent way to be able to predict the rise and bounce of bubbles. We start by describing a bubble rising in bulk that reaches constant speed, where buoyancy and drag balance each other.

3.1. Bubbles rising in bulk

For a bubble rising at constant speed the only two forces are buoyancy and drag in the force balance of Eq. (5) resulting in

$$\frac{4}{3}\pi R^3 \rho g = C_d Re \frac{\pi}{4} \mu R V \tag{30}$$

In this balance we have neglected forces due to acceleration, i.e. added mass [66,67] and history force. We will discuss the drag force in the next section in more detail.

3.1.1. Drag force for high Reynolds numbers

It is clear from the discussion of Section 2 that a theory without viscous forces will not be able to explain the terminal velocity of a bubble, let alone the interaction with a wall. In potential flow, a non-accelerating free particle does not have a drag, the so-called d'Alembert paradox [68]. The viscous force that we have already discussed in Eq. (9) is the drag force $\mathbf{F}_D$. Contrary to the relatively simple analytical expressions for the drag force for Stokes flow, Eq. (9), for high Reynolds flow the drag force is a complicated function of the Reynolds number (Eq. (3))

$$\mathbf{F}_D = C_D Re \frac{\pi}{4} \mu R V \ \mathbf{k} \tag{31}$$

Here Re is expressed as a function of the instantaneous velocity of the centre of mass, V (not necessarily the terminal velocity V_T). Traditionally the drag force is expressed as a function of the drag coefficient C_D, defined as

$$C_D = \frac{|\mathbf{F}_D|}{\pi R^2 \frac{1}{2} \rho V^2} \tag{32}$$

in which $\rho V^2/2$ represents the dynamic pressure (from the Bernoulli equation) and πR^2 the frontal area of the bubble.

When a bubble with mobile interface rises in a liquid at large velocity it deforms. Moore [69] obtained the drag coefficient for an ellipsoidal bubble as

$$C_D Re = 48G(\chi)\left(1 + \frac{H(\chi)}{\sqrt{Re}}\right) \quad (33)$$

where χ is the aspect ratio of the larger axis R_H to the smaller axis R_V of the bubble (as defined in Fig. 12). The functions $G(\chi)$ and $H(\chi)$ are given by

$$G(\chi) = \frac{1}{3}\chi^{4/3}(\chi^2-1)^{3/2}\frac{\left[\sqrt{(\chi^2-1)}-(2-\chi^2)\cos^{-1}(1/\chi)\right]}{\left[\chi^2\cos^{-1}(1/\chi)-\sqrt{(\chi^2-1)}\right]^2} \quad (34)$$

and [70]

$$H(\chi) = 0.0195\chi^4 - 0.2134\chi^3 + 1.7026\chi^2 - 2.1461\chi - 1.5732 \quad (35)$$

A relation between the aspect ratio χ and the Weber number (Eq. (4)) that takes the form [71,72]

$$\frac{R_V}{R_H} = \frac{1}{\chi} = 1 - \frac{9}{64}We \quad (36)$$

has been proposed for bubbles rising in bulk. Eq. (36) can easily be obtained by a Taylor expansion using the pressure distribution on a sphere linked with the Laplace pressure and surface deformation [72]. This result is very accurate for $We < 3.5$ when compared to experimental data (see Figs. 13 and 14).

If the bubble has a tangentially immobile boundary condition, the velocity is lower, the bubble remains spherical with negligible deformation and the drag coefficient obeys the classical empirical result of Schiller and Naumann [73] for a solid sphere

$$C_D Re = 24(1 + 0.15Re^{0.687}) \quad (37)$$

Carefully conducted experimental measurements by Duineveld [74], by adding different surfactant concentrations of Triton X_{100}, $Brij_{30}$ and SDS show that for larger surfactant concentrations, the bubble rises like a solid sphere.

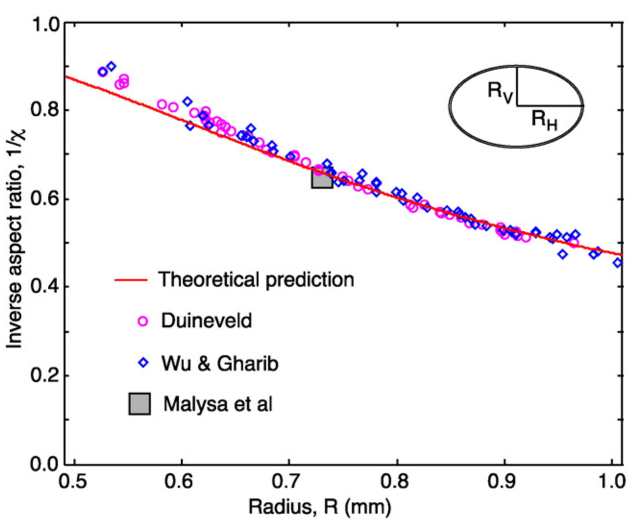

Fig. 13. Comparison between experiments [21,25,75] and theory for the bubble aspect ratio, $\chi = R_H/R_V$ as a function of equivalent radius for clean bubbles. The inset shows the definition of R_V and R_H. Small bubbles will have an aspect ratio of 1.0, as the bubble radius increases the shape becoming more and more ellipsoidal.

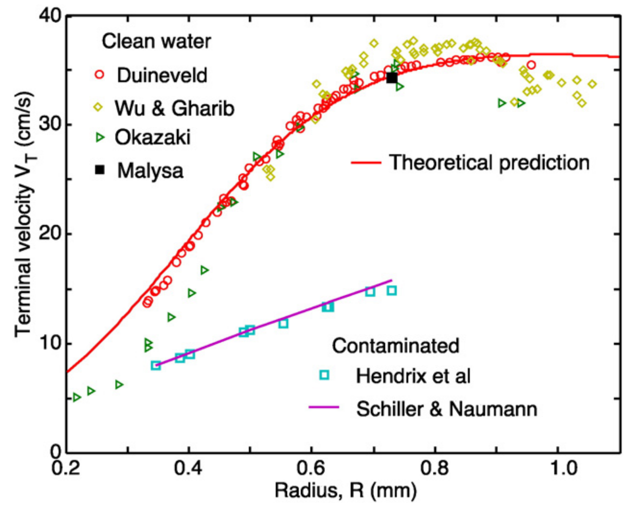

Fig. 14. The terminal velocities from experiments of Duineveld [75], Okazaki [76], Malysa [25] and Wu and Gharib [21] are compared with theory. Experimental results of Hendrix et al. [9] (open squares) agree with the results for immobile spheres from the empirical formula of Schiller and Naumann [73] (Eq. (37)). Note that for this 'inertial' regime, the terminal velocity for 'mobile' bubbles (clean) is more than twice that of 'immobile' bubbles (contaminated).

3.1.2. Comparison between theory and experiments for terminal speed and deformation

The aspect ratios as a function of bubble radius for different experiments [21,25,75] are compared with theory (Eqs. (31)–(36)) in Fig. 13. Note that the deformation becomes larger for increasing bubble size.

The terminal velocity for a clean system considering various experiments [25,75,76] and theory (Eqs. (31)–(36)) where the bubble interface behaves as mobile is given in Fig. 14. The maximum at $R \sim 0.75$ mm can be explained from a physics point of view, since a considerable increase of the frontal area occurs, which in turn increases the drag.

The terminal velocities obtained by Hendrix et al. [9] are also plotted in Fig. 14 and agree with the solid sphere result (Eq. (37)) suggesting an immobile boundary condition at the bubble surface. In Hendrix et al. [9], de-ionized water was used under standard laboratory conditions. To obtain terminal velocities that agree with a fully mobile interface, extreme care has to be taken in the whole process to prevent any surface-active material to remain in the water. Small concentrations are enough to change the boundary condition from mobile to immobile.

The results presented in Fig. 14 correspond to bubbles that rise with a straight path. Larger bubbles bigger than about 1 mm in radius would present helical of zig-zag path during rise. Careful experiments have been performed to explain different aspects of non-straight bubble rise [77,78]. Most numerical simulations are based on a fixed non-spherical bubble and analyse the drag and vortex shedding (which is not symmetric) that causes the bubble not to rise straight [79,80]. The focus of the current review is on bubbles that rise in a straight path.

3.2. Bubbles impacting on a surface

For the case of a large bubble impacting a surface some additional forces need to be taken into account. Besides buoyancy and drag, the balance of forces (Eq. (5)) now also contains $\mathbf{F}_A$ the added mass force, $\mathbf{F}_H$ the history force and $\mathbf{F}_F$ the film force due to a lubrication pressure build up in the film between the bubble and the surface.

Besides the usual added mass force in an unbounded domain, an additional contribution that only acts near the surface appears. The history force needs to be included for the immobile boundary condition (termed "immobile bubbles") and we take the same form as the one in the previous section (Eqs. (11) and (12)a), but can be neglected for the mobile boundary condition [59]. We first give the final form of the force balance for mobile and immobile bubbles and then derive the new forces individually.

3.2.1. Bubble with tangentially immobile surface

The balance of forces for immobile bubbles will result in the following equation

$$\frac{4}{3}\pi R^3 \rho C_m \frac{dV}{dt} = \frac{4}{3}\pi R^3 \rho g - C_d Re \frac{\pi}{4}\mu RV + \frac{2}{3}\pi R^3 \rho \frac{dC_m}{dH} V^2 - 6\sqrt{\pi\mu\rho}R^2 \int_{-\infty}^{t} \frac{1}{\sqrt{t-\tau}}\frac{dV}{d\tau}d\tau - \int_0^{\infty} 2\pi r p_F \, dr \tag{38}$$

This equation can be solved by numerical means. The term on the left hand side together with the third term on the right hand side represent two contributions to the added mass force $\mathbf{F}_A$ which will be derived in Section 3.2.3. Buoyancy $\mathbf{F}_B$ and drag $\mathbf{F}_D$ are represented by the first and second terms on the right hand side with C_DRe given by Eq. (37). The fourth term is the history force $\mathbf{F}_H$ (derived from Eqs. (11) and (12)a for the immobile case). The last term represents the film force $\mathbf{F}_F$ which will be derived in Section 3.2.4. It is essentially the integral of the lubrication pressure p_F over the film area [70]. In Section 3.4 we compare results from this equation and experimental data of bouncing bubbles.

3.2.2. Bubble with mobile surface

Mobile bubbles have a much higher approach velocity than immobile bubbles (see Fig. 14). For example a bubble with radius $R =$ 0.6 mm will rise with about 13 cm/s if the surface is immobile, while it will attain 30 cm/s for a mobile surface.

The equation of motion for a bubble with a mobile interface is almost identical to Eq. (38)

$$\frac{4}{3}\pi R^3 \rho C_m \frac{dV}{dt} = \frac{4}{3}\pi R^3 \rho g - C_d Re \frac{\pi}{4}\mu RV + \frac{2}{3}\pi R^3 \rho \frac{dC_m}{dH} V^2 - \int_0^{\infty} 2\pi r p_F \, dr \tag{39}$$

Note that the history force can be neglected for the mobile boundary condition at the bubble interface [59] and C_DRe is now given by Eq. (33).

3.2.3. Added mass force

We can obtain the added mass force $\mathbf{F}_A$ using an energy approach. The kinetic energy of the system is defined as

$$E = \frac{1}{2}V^2 \frac{4}{3}\pi R^3 (\rho_b + C_m \rho) \tag{40}$$

Since we are dealing with bubbles in water, the density of the air contents of the bubble ρ_b is much smaller than the density of the surrounding liquid ρ; we can neglect the term with ρ_b here. For a drop in another liquid, both densities are needed. The work done per unit time on the system can be described by:

$$-V\mathbf{F}_A = -\frac{dE}{dt}\ \mathbf{k} = -\rho \frac{4}{3}\pi R^3 \left(C_m V \frac{dV}{dt} + \frac{1}{2}V^2 \frac{dC_m}{dH}\frac{dH}{dt} \right)\ \mathbf{k} \tag{41}$$

(with $dC_m/dt = dC_m/dH\ dH/dt$). For a spherical bubble approaching a surface [81,82], the force can thus be written as (noting that $dH/dt = -V$)

$$\mathbf{F}_A = \left(\rho \frac{4}{3}\pi R^3 C_m \frac{dV}{dt} - \frac{1}{2}\rho \frac{4}{3}\pi R^3 \frac{dC_m}{dH} V^2 \right)\ \mathbf{k} \tag{42}$$

which explains the two separate contributions in Eqs. (38)–(39). In our model H is taken to be the film height between the bubble and the wall at the axis of symmetry (even if deformation is present). The first term on the right hand side of this equation represents the classical added mass force (Eq. (10)) and it depends on the acceleration of the bubble. It is a typical 'inertial' force; it does not give any damping to the system.

The second term arises from the fact that the added mass coefficient C_m changes when the bubble approaches the wall. It is proportional to V^2 and thus always points in the direction away from the wall (no matter if the bubble is approaching or retracting). This also implies that it is not contributing to the damping of the system; it is a purely inertial force since it has its origins in potential flow theory.

An approximate expression for C_m was given by Kharlamov et al. [82] and will be used here. With $\zeta = (H + R) / R$, this approximation reads

$$C_m = \frac{1}{2} + 0.19222\zeta^{-3.019} + 0.06214\zeta^{-8.331} + 0.0348\zeta^{-24.65} + 0.0139\zeta^{-120.7} \tag{43}$$

Since the bubble will attain a shape which very closely approaches that of a sphere shortly after 'feeling' the wall, we have not included non-spherical effects of the added mass coefficient in this study i.e. the factor 1/2 remains the same. C_m is plotted as a function of H/R in Fig. 15. It reverts back to the classical result $C_m = 1/2$ as ζ becomes large. For $\zeta = 1.0$ ($H = 0$, or a touching bubble), its value becomes $C_m = 0.803$. An analytical solution for $dC_m/d(H/R)$ has been derived by Miloh [81]. A comparison of the (exact) solution of Miloh [81] and the approximation (used in this work) based on Eq. (43) is also given in Fig. 15.

3.2.4. Film force based on lubrication and film deformation

As mentioned during the discussion on the drag force, the influence of the wall is not included in Eq. (31) (except for the fact that the velocity V changes during approach, resulting in a different drag force). If the bubble is getting closer to the wall, a water film is being formed which creates an effective barrier for the bubble to advance. This film is pushed forward and the film 'drains' under the pressure p_F that this is generating. It turns out that a good approximation for p_F can be obtained using lubrication theory (see Hendrix et al. [9]). Surface tension also plays an active role in the lubrication process (since it 'pushes' the film) and deformation due to surface tension must be taken into account. A full description of the lubrication–film deformation model is given next. It suffices to mention here that the force thus generated on the bubble

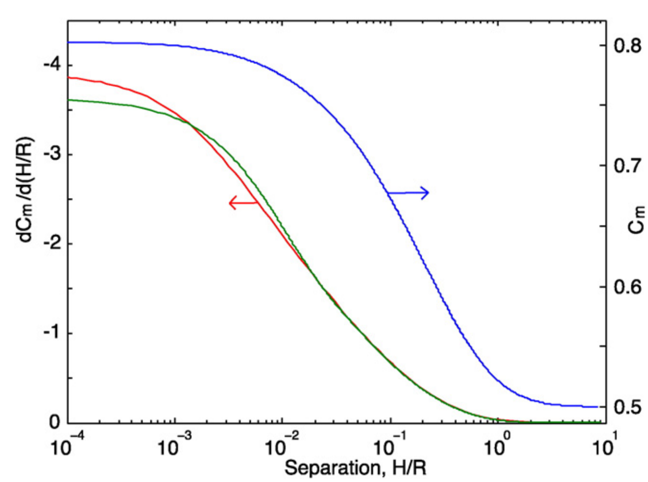

Fig. 15. Added mass coefficient C_m as a function of H/R (blue curve). Also plotted is $dC_m/d(H/R)$. Note that $dC_m/d(H/R) < 0$. The approximate theory of Kharlamov [82] is indicated with the green curve, while the exact solution of Miloh [81] is given in the red curve.

can be obtained by integrating the pressure p_F over the (axial symmetric) film domain as

$$\mathbf{F}_F = \int_0^\infty 2\pi r p_F dr \ \mathbf{k} \tag{44}$$

The integral is extended to infinity since p_F decays to zero as $1/r^4$ [83]. However, for most cases the pressure builds up in a region smaller than the bubble radius and decays very fast. A positive sign appears in Eq. (44), since the film force is pushing the bubble down (and thus acts opposite to the buoyancy force). The film force has both a damping effect (due to the viscosity of the film), and an elastic effect (surface tension effectively stores energy during the deformation of the bubble). At first sight, it might seem that the viscous effects of Eqs. (31) and (44) are double counted, but one should realize that Eq. (31) does not take into account any wall effects. Furthermore, it will be shown later, when the forces are actually calculated that either the drag force $\mathbf{F}_D$ or the film force $\mathbf{F}_F$ is dominant. This is due to the fact that the velocity is almost zero when the film is formed and the film force is almost zero when the velocity is not.

If the film Reynolds number is smaller than unity the film is under Stokes flow. Assuming that the problem remains axisymmetric, and that the film height is much smaller than the bubble size, the Navier–Stokes and continuity equations, Eqs. (1) and (2) can be simplified to the lubrication form

$$\frac{\partial p_F}{\partial r} = \mu \frac{\partial^2 u_r}{\partial z^2} \tag{45}$$

$$\frac{\partial p_F}{\partial z} = 0 \tag{46}$$

$$\frac{\partial u_z}{\partial z} = -\frac{1}{r}\frac{\partial (r u_r)}{\partial r} \tag{47}$$

where u_r and u_z are the velocity components in the r (radial) and z (vertical) directions. Since the pressure does not depend on the z-coordinate according to Eq. (46), u_r can be solved with Eq. (45) and will give a quadratic velocity profile. Taking into account the boundary condition $u_r = 0$ at the water–solid interface and at the air–water interface (for an immobile bubble), we will get a parabolic velocity profile as shown on the left in Fig. 2. If on the other hand the air–water interface cannot sustain a shear stress, the half parabolic velocity profile shown on the right of Fig. 2 will be obtained. If the obtained function u_r is substituted into Eq. (47) and integrated from 0 to the film height h, we will get an expression for dh/dt.

After some algebraic manipulation, the classical film drainage equation or Stokes–Reynolds model can be derived in axial symmetric form [7,83,84]

$$\frac{\partial h}{\partial t} = \frac{c}{12\mu r}\frac{\partial}{\partial r}\left(r\ h^3 \frac{\partial p_F}{\partial r}\right) \tag{48}$$

where the constant $c = 1$ corresponds to an immobile boundary condition at the air water interface and $c = 4$ for a mobile condition. Note that the film height h is (besides time) a function of the radial coordinate r; the film is in general not flat, nor can it be assumed to be 'quasi-flat' (a discussion on this issue can be found in Chan et al. [85]).

If the film would not deform, Eq. (48) would give rise to a pressure that is ever increasing. In practice however, the surface tension will not be able to keep up with high pressures and the actual pressure in the film will be around or slightly above the Laplace pressure $2\sigma/R_L$, where R_L is the Laplace radius ($R_L \sim R$), σ is the interfacial tension. We assume that the deformation is governed by the Young–Laplace equation that relates the mean curvature of a fluid interface to the pressure difference across the interface of the bubble under quasi-equilibrium conditions. Besides the Laplace pressure ($2\sigma/R_L$) between the two sides of the curved interface, we consider two additional contributions to the pressure difference, the hydrodynamic pressure p_F, due to the drainage of the aqueous thin film between the bubble and the surface and the disjoining pressure Π on the interface [63]. If the bubble deformations are axially symmetric, the pressure p_F in the film obeys the Young–Laplace equation of the form [4,5,63,86]

$$\frac{\sigma}{r}\frac{\partial}{\partial r}\left(r\frac{\partial h}{\partial r}\right) = \frac{2\sigma}{R} - \Pi - p_F \tag{49}$$

where Π is only relevant when the separation becomes really small ($h < 0.1$ μm) just before bubble adhesion. We need one initial condition

$$h(0,\ r) = H_0 + \frac{r^2}{2R} \tag{50}$$

where H_0 is the initial separation and time $t = 0$ is taken at a position where the bubble rises at its approach velocity and the deformation due to the wall can be neglected. The initial profile as given in Eq. (50) will give rise to a zero pressure $p_F = 0$ when substituted in Eq. (49).

We also apply four boundary conditions. Due to symmetry $\partial p_F/\partial r = \partial h/\partial r = 0$ at $r = 0$. For the far-field boundary conditions we assume that the pressure decays as $1/r^4$ [83] to write $r\partial p_F/\partial r + 4p_F = 0$ at $r = r_{max}$. The last boundary condition assumes that $dh/dt = -V(t)$ at $r = r_{max}$ [87]. Once we calculate V from Eqs. (38) or (39) we use it as the boundary condition for the lubrication equations. In the simulations we used as interfacial tension $\sigma = 72$ mN/m and the viscosity of water as $\mu = 1.0$ mPa·s.

In order to test the above lubrication model, the authors have taken the $V(t)$ from the experiment and simulated the film height, which was then compared to experimentally obtained data [9]. Alternatively, we can predict $V(t)$ from Eqs. (38) or (39), resulting in a model without any fitting parameters. This is done in Section 3.4.1 for the immobile film drainage and in Section 3.4.2 for mobile film drainage (as experimental comparison we have used the data from the Malysa group [47]).

3.3. Experiments with bouncing bubbles

A great deal of research has been devoted to the impact of millimetre-sized bubbles with surfaces. Most experimental work that concerns bouncing bubbles is restricted to side images of rise and impact [25,39,43,44]. The process of thin film drainage is not observed in those experiments. An experimental challenge for this system is the widely different length scales that are present. Bubbles of millimetre size form films that are on the micro to nanometre scale.

An innovative approach was used by Hendrix et al. [9]. In their experiment, a millimetre size bubble is released from a needle and rises under buoyancy against a horizontal glass surface. A schematic of an experimental setup of a bubble that was rising under gravity before hitting a surface together with a photograph of such a bubble is presented in Fig. 16. A high-speed camera captures the trajectory and shape of the rising bubble and a synchronized camera records the evolution of the film thickness between the bubble and the glass surface by following the interference fringe pattern.

A typical set of experimental results is shown in Fig. 17. The top sequence shows the interferometric photographs at selected stages of interaction: bubble rise stage (Fig. 17a), impact and dimple formation (Fig. 17b), film rupture (Fig. 17c) and three-phase contact line expansion to a final position where the bubble is attached to the glass (Fig. 17d). We notice that while the film changes continually in the top view, the corresponding side view images at the bottom sequence show that the centre of mass of the bubble barely moves (bottom sequence of Fig. 17b–d).

In Fig. 18, we show a typical fringe evolution when a bubble first impacts on the glass surface. The interferometric fringes are (almost)

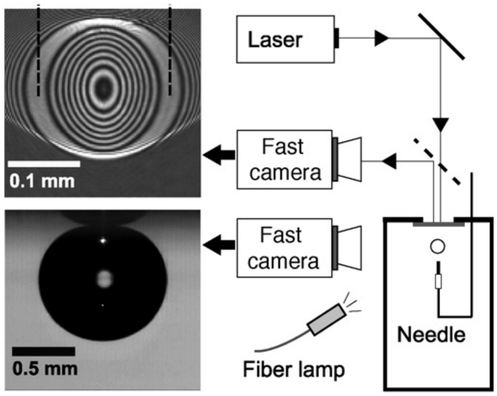

Fig. 16. Schematic of the experimental setup of Hendrix et al. [9] combined with photograph of a bubble impacting a surface, $R = 400$ μm as well as interferometric fringes.

always circular indicating that the film exhibits axial symmetry. In less than 2 ms the bubble approaches and inverts its curvature in the film region to form a so-called 'dimple'. For deformable bubbles, a dimple forms if the pressure in the film becomes higher than the Laplace pressure of the bubble. The conversion from fringes to separation is indicated on top of Fig. 18. To obtain the experimental film thickness $h(r,t)$, we use Bragg's equation [88] for a fringe of order m: $h = m\,\lambda_L/(2\,n)$, where $\lambda_L = 532$ nm is the wavelength of the laser and $n = 1.33$ is the refractive index of water. This equation indicates that in practical terms, the difference in separation between two white fringes is about 200 nm. The relative film profiles can now be reconstructed as a function of radial coordinate and time. The absolute separation is obtained from the point of contact when the film ruptures and the bubble adheres to the surface. After that, we count backwards to produce the time evolution of the absolute separation and the bubble shape.

The purpose of the interferometric measurement is to: (1) measure the film height and (2) ascertain that the film drainage process is axial symmetric (circular fringes) thus axial symmetric theory can be used. Note that measurements based on intensity, although feasible, must be interpreted with extreme care. The small sizes of these bubbles ensure a straight vertical rise path and axisymmetric bubble deformation resulting from interaction with the glass plate.

3.4. Comparisons between experiment and theory on bouncing bubbles

3.4.1. Bubbles with tangentially immobile surface and drainage

The next stage in this review is to test the constructed theory against experimental data. Even though lubrication theory is known to be quite sturdy [89], it is by no means obvious that it will still be accurate under the current conditions. By analysing the experimental videos the trajectory of the bubbles was obtained. The velocity of the centre of mass $V(t)$ can thus be obtained. In Fig. 19 we present the experimental velocity of the centre of mass for different bubble sizes as symbols (Hendrix et al. [9]). Two different representative experiments were chosen, one bubble with radius $R = 385$ μm and another with $R = 630$ μm. As can be expected, the bigger bubble has a larger approach velocity and also exhibits a larger bounce (both in period and in amplitude). In Hendrix et al. [9] and Manica et al. [51], the lubrication model of Eqs. (48)–(50) was solved using the experimental $V(t)$ as input for the model.

In this section, we will use the force balance model (Eq. (38)), together with the drainage equations (Eqs. (48)–(50)) with $c = 1$ solved simultaneously [90]. The numerical results are represented as solid lines in Fig. 19. The agreement is good taking into account the simplicity of the model and the fact that there are no fitting parameters in the model.

The comparison between numerical simulations of the force balance–lubrication theory and the experiment of Hendrix et al. [9] concerning the film heights is shown in Fig. 20a for immobile boundary condition at the air–water interface. The agreement is impressive all the way to film rupture. A dimple first appears at $t \sim 9$ ms and disappears again around $t = 12$ ms. During this period the film height is thinnest not at the centre, but at a circular region, termed a 'rim'. The rim reaches a maximum value of about 75 μm. Fig. 20b shows the spatiotemporal evolution during the first impact and the drainage process of a few milliseconds. It clearly shows that the film is axial symmetrically draining, which was the case for all the experiments that were analysed. The dimple disappears during a short period from $t = 12$ to 14 ms. It then reappears and remains all the way to film rupture. In Hendrix et al. [9], the results were analysed with the lubrication theory only by feeding $V(t)$ as a boundary condition to Eqs. (48)–(50). The results of the two approaches are quasi-indistinguishable.

The forces obtained from the coupled force-lubrication approach are plotted in Fig. 21. Most of the action occurs during the first impact while later on everything settles. Initially ($t < 0$ ms) buoyancy is balanced by

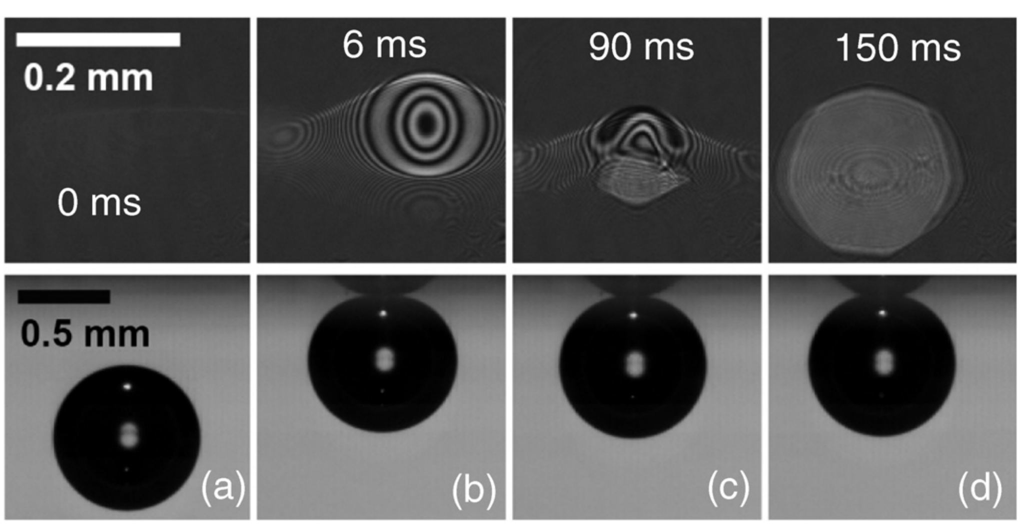

Fig. 17. Selected movie frames highlighting (a) bubble rise, no fringes are observable (b) interaction with the glass plate, with formation of interference fringes (c) film rupture and (d) three-phase contact line formation. The top sequence corresponds to interferometric data from a first camera while the bottom sequence represents side view images taken at the same time instants by a second camera. The bubble radius is $R = 400$ μm and the experimental times corresponding to the sequence (a) to (d) are $t = 0$, 6, 90 and 150 ms. The film rupture is clearly a non-axial symmetric event.

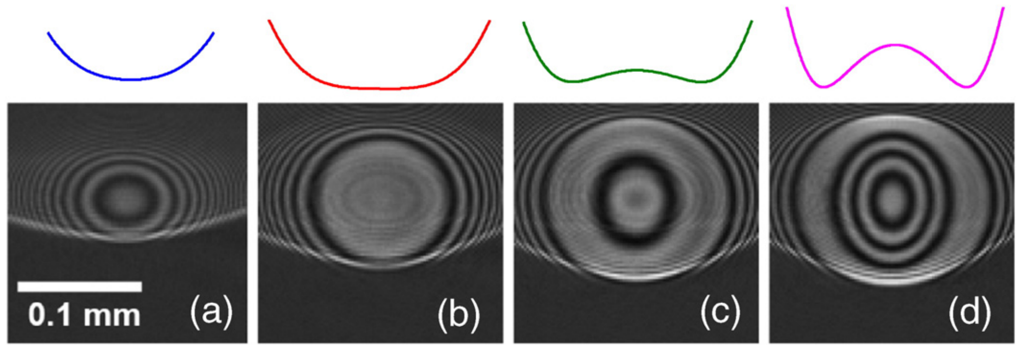

Fig. 18. Typical sequence of interferometric fringes for a time-step of 0.37 ms between frames during the first contact of the bubble of $R = 400$ μm against the glass surface. (a) Bubble approach; (b) flattening of the bubble surface; (c) curvature inversion or dimple formation; (d) dimple grows. The actual film shapes have been plotted above each frame.

the drag force and once inertial effects are gone buoyancy is balanced by the film force ($t > 200$ ms).

From Fig. 21 it is evident that the most important contribution to the bubble bounce originates from the film force. More details as well as a different example for a larger bubble can be found in Klaseboer et al. [90].

3.4.2. Bubbles with mobile surface and drainage

Experiments with bubbles rising under clean surface conditions and bouncing from various surfaces have been performed extensively by the group of Malysa [41,42,45–47]. The bubble velocity is obtained with the force balance model of Eqs. (39) and (48)–(50) with $c = 4$ and compared against the experiments of Kosior et al. [91]. In Fig. 22a we compare a typical experiment. More details can be found in Manica et al. [92]. Since the deformation is very large for this kind of bubbles, we have taken $r_{max} = 1.2R$ for the first part of the simulation and $r_{max} = 0.9R$ after $t = 25$ ms. The value of the aspect ratio, χ, used in Eq. (33) is calculated to be $\chi = 1.52$. It is then changed to $\chi = 1$ at the time marked with a square in Fig. 22a because the bubble is observed experimentally to remain nearly spherical after the first impact. The agreement is impressive, especially when it is realized that our model does not contain any fitting parameters. Unfortunately, no experimental data concerning the film thickness is available. We have plotted the numerical film thicknesses (both at the centre h_0 and at the rim h_m) for this case in Fig. 22b. The results of the previous sections give us confidence that the constructed theory is probably giving the right answer. If this is indeed the case, the film height during the first bounce reaches a minimum value of about 4 μm.

We can see that during subsequent bounces the phenomena are similar. Eventually the bounces stop and only film drainage remains all the way to film rupture. Five distinct dimples can be observed.

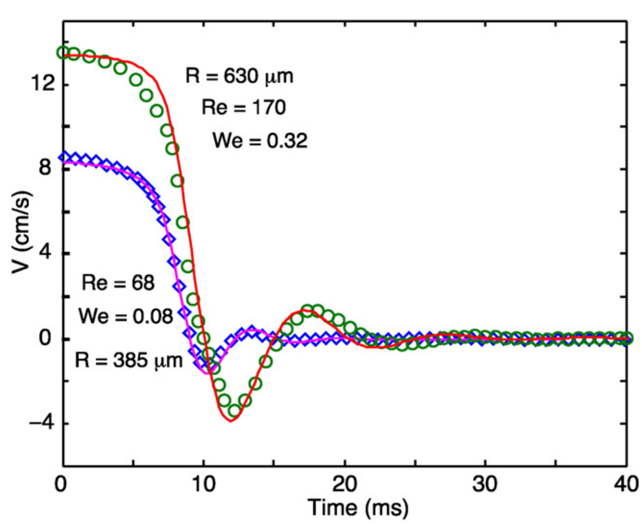

Fig. 19. Comparison between force balance model (continuous lines Eq. (38)) and experiment for immobile bubble with immobile drainage (symbols) for two different bubbles with size $R = 385$ and 630 μm. Both curves show a 'damped oscillator' response. The origin of time is taken arbitrary. The Reynolds and Weber numbers based on the approach velocity V_T are also indicated.

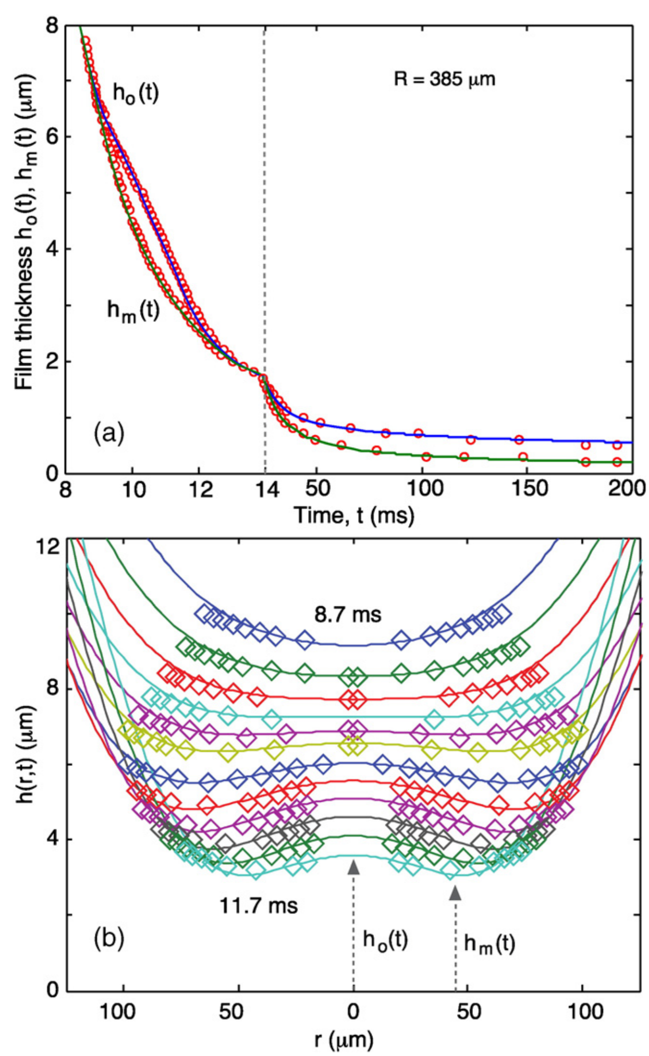

Fig. 20. Comparison between theory and experiment for the height at the centre and at the rim for a bubble with $R = 385$ μm (from Fig. 19) using the immobile boundary condition, $V_T = 8.7$ cm/s. Note that the scaling of the time axis is changed at $t = 14$ ms. (b) Spatial evolution of the film profile during first impact from 8.7 to 11.7 ms.

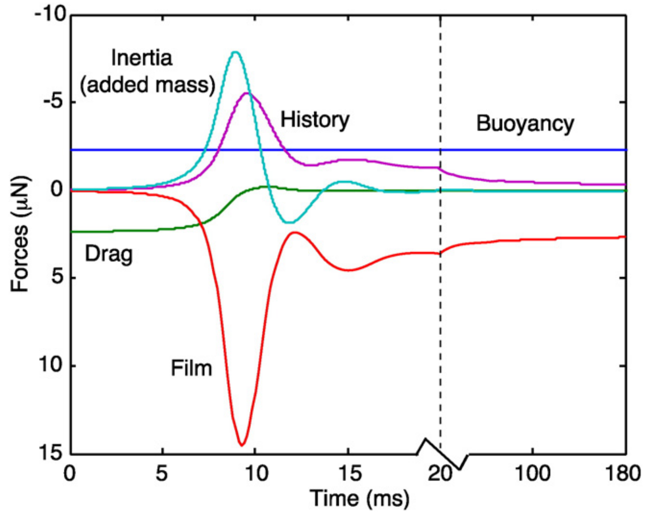

Fig. 21. The forces as a function of time for a bubble with $R = 385$ μm (from Fig. 19) according to the force balance model. The sum of all forces is (necessarily) zero. Far away from the wall, buoyancy balances drag. For larger times ($t > 200$ ms), buoyancy and the film force compensate each other.

The evolution of forces as a function of time for this case is shown in Fig. 22c and has some interesting features. The film force becomes positive for several short periods, which means that there is a "suction effect" which can cause film rupture in some cases if the film is thin enough. However, from Fig. 22b we can see that the film thickness remains well above 1 μm during the bouncing process.

4. Discussion

4.1. The remarkable success of lubrication theory

If due care is taken, deformable thin films can be modelled surprisingly accurately with lubrication theory, ranging from the modelling of a thin film in a Taylor bubble [93–95] to air lubrication between a deformable tape and a recording head [89]. This is somewhat surprising since the global Reynolds number (Re) is much larger than one. It must be remembered though that the film Reynolds number very quickly becomes smaller than one and lubrication theory (combined with surface deformation) can describe an important part of the physics of the problem. Furthermore, it has been shown in this review that if the velocity of the centre of mass is given as input for the lubrication equations through a force balance, a theory without any fitting parameters is capable of predicting the experimentally measured film heights as well as the bouncing behaviour of the bubble.

4.2. Some remarks on mobile and immobile surfaces

In this article we have seen several times different boundary conditions on the bubble surface (mobile or zero tangential stress vs immobile or zero tangential velocity). In this section we describe a rather peculiar experiment in which the bubbles rise under immobile boundary conditions, but appear to exhibit film drainage with mobile conditions [10]. In Fig. 23 we compare the results for two bubbles with approximately the same radius (625 and 630 μm), the same approach velocity (V_T ~ 13.5 cm/s), yet exhibiting an entirely different bouncing behaviour after 10 ms. One bubble has a much more oscillating behaviour than the other. The film heights were measured simultaneously with the velocity of the centre of mass and are shown in Fig. 24. We attribute this difference to the surface mobility in the film area. If the bubble is (partly) clean, it is most likely to be in the frontal area, since all the surfactants are swept to the back and the film area might remain clean enough to exhibit mobile interface behaviour. This result is consistent

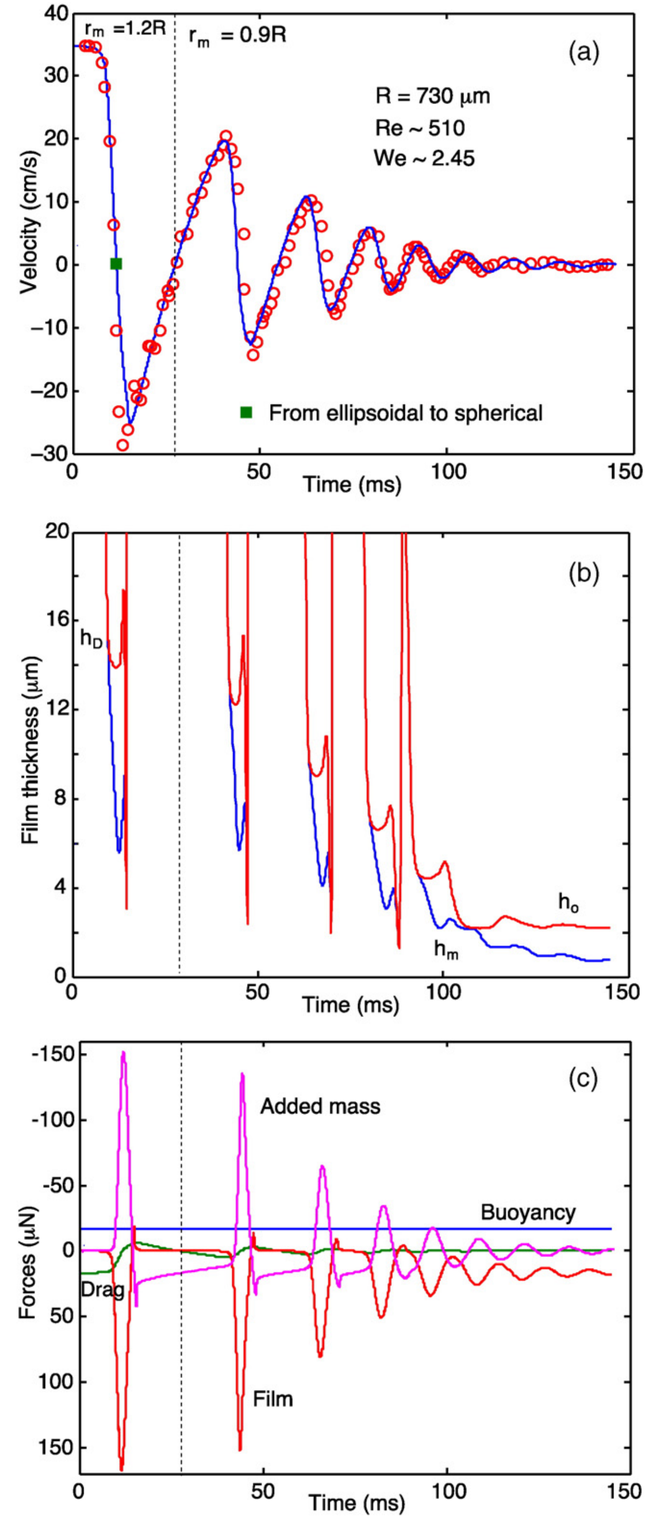

Fig. 22. (a) The velocity of the centre of mass of the bubbles of Eq. (39) as a function of time compared to experiments of Kosior et al. [91] for a bubble with radius $R = 730$ μm and approach velocity $V_T = 35$ cm/s. It has mobile boundary conditions during rise, film drainage and bounce. (b) Film thickness at the centre, h_0, and at the rim, h_m, during subsequent bounces (numerical results). (c) Time evolution of the forces (numerical).

with experimental data of Malysa et al. [25] and numerical simulations of Cuenot et al. [31]. From experiments similar to Fig. 23, the bouncing behaviour can give us further clues on the state of the film–bubble interface; mobile or immobile. If the bubble is entirely covered with surfactants, the whole bubble will be immobile (including the film area).

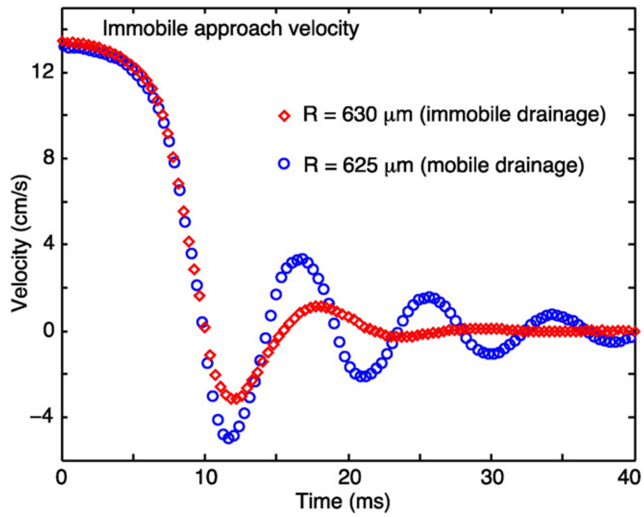

Fig. 23. Experimental velocity of the centre of mass against time for bubbles of similar size with similar approach velocity (V_T ~ 13.5 cm/s, corresponding to an immobile interface), yet presenting significantly different bouncing behaviour. The Reynolds number (based on approach velocity) and Weber number are almost identical for both cases Re ~ 165 and We ~ 0.30, indicating that these two parameters are not the only ones governing the dynamics of the system. The difference is attributed to the thin film boundary condition (immobile or mobile drainage).

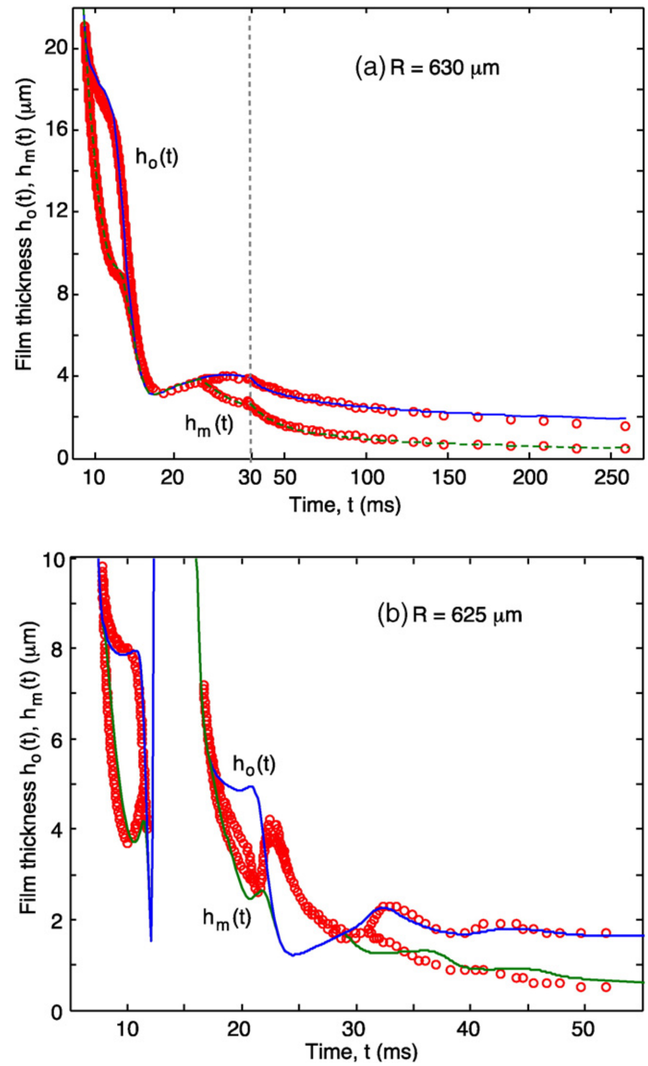

Fig. 24. Comparison of bouncing behaviour for two almost identically sized bubbles R ~ 630 μm and approach velocities (V_T ~ 13.5 cm/s see Fig. 23), but with different mobility conditions at the film–bubble interface (a) immobile and (b) mobile. The red circles represent the experimentally measured film heights at the centre (h_0) and the thinnest film height (h_m). See Fig. 20 for definition of h_0 and h_m. Note the substantially qualitative different behaviour of the film drainage.

Surface mobility plays a crucial role in the dynamical behaviour of the bubble. It enters the physics of the problem in three different ways. First of all, as we have seen in Fig. 14, the rise velocity can be affected. However, a spherical cap bubble can still rise with (almost) the same speed as a 'clean' bubble. During the film drainage process, a draining film with a mobile interface will be substantially different from the drainage of an immobile interface. As could be expected intuitively, a mobile film drains much faster (a factor of 2; see Eq. (48) with $c = 1$ or 4). Finally, mobility can affect even the importance of the history force, due to its close relationship with the boundary layer around the bubble.

In Fig. 24 the experimental as well as the numerical minimum film height and the height at the centre (at $r = 0$) are shown. By setting $c = 1$ or $c = 4$ in Eq. (48) we can simulate an immobile and a mobile film interface respectively, while keeping all other parameters the same. We see that the immobile bubble (Fig. 24a), forms a film and the film keeps on thinning except for a small period around $t =$ 25 ms. On the other hand, the mobile bubble (Fig. 24b) forms a film, but then the whole profile detaches around $t = 12$ ms. In both the experiment and the numerical simulation, the film essentially disappears at that instant (the experimental interference fringes even disappear here). Also note that the first appearance of the dimple appears at values of 19 μm and 8 μm for the immobile and mobile drainage cases respectively. In conclusion, it thus turns out that 'mobile draining bubbles' exhibit much less damping, but the film heights attained are roughly a factor of two less than their immobile counterparts during the first impact. Thus, all other parameters remaining the same, the surface mobility of the film has a real influence on the global bouncing behaviour as clearly illustrated in Figs. 23 and 24.

4.3. Extreme film thinning just before rebound

When rebound occurs, a peculiar phenomenon can be observed. From the experiment as well as theory, as the outside of the bubble is already retracting, the film still keeps thinning. This is obvious from Fig. 22b or 24b, where the main part of the bubble is moving away from the wall, while the central part is still thinning. Just before this part of the bubble is also retracting, the centre of the bubble becomes very thin in a very small amount of time ($\ll$1 ms) and then immediately becomes very large (this corresponds to the sharply pointed profile observed in Fig. 22b at t ~ 15 ms and in Fig. 24b at t ~ 12 ms). The movement of the film and the movement of the bubble itself can thus be in opposite directions. This can even result in a negative film pressure (i.e. a suction, such as observed in Fig. 22c at $t = 15$ ms during a fraction of a millisecond). If the film becomes thin enough during this process, it can actually lead to film rupture. This phenomenon was also observed during the coalescence of bubbles in AFM [96], drops in a four-roll mill [97], in microfluidics channels [98] and in shear flow [99]. This phenomenon can be explained theoretically [100,101].

4.4. The relation between bounce time and relaxation time

There is still one more aspect of the physics that we can explore. The typical 'bounce-time' for a bubble appears to be closely related to the so-called relaxation time. Far away from the surface, even during rebound, surface forces can be neglected, and assuming the history force contribution is not too large, Eqs. (38) and (39) essentially reduce to

$$\frac{4}{3}\pi R^3 \rho C_m \frac{dV}{dt} = \frac{4}{3}\pi R^3 \rho g - C_d Re \frac{\pi}{4}\mu RV \tag{51}$$

When the left hand side of Eq. (51), the added mass force, with $C_m = 1/2$, is compared to the buoyancy force, a typical time scale for the system can be derived (a typical velocity scale is V_T), the relaxation time

$$t_R = \frac{V_T}{2g} \tag{52}$$

For example, if we take as a typical oscillation period to be the time elapsed between the first and second minimum in the velocity–time graphs, then we see that this period is about $2t_R = V_T/g$. The factor '2' appears since it takes two 'relaxation times' to bounce back and return to the surface again. For example in Fig. 19, the bounce time is about 11 ms for the bubble with $R = 630$ μm, while $2t_R \sim 13.8$ ms. For the second bubble with $R = 385$ μm, the bounce time is 7 ms, while $2t_R \sim 8.2$ ms. This 'law' is also observed in Fig. 22a (35 ms vs $2t_R \sim 36$ ms).

It seems as if the physics of the problem is decoupled in two distinct phases. First of all, the film with its drainage, which forms a dimple, which appears to depend on the approach speed. Secondly, the inertia of the bubble itself, which results in a bounce time which is related to the relaxation time of the bubble. Of course, when the bubble becomes smaller the viscous effects become more dominant (as in Section 2) until no bounce will be observed anymore.

4.5. Solid surface vs air–water interface

It is interesting to note that the bouncing behaviours for bubbles against a free surface and a solid surface appear very similar. In Fig. 25 we compare experimental data extracted from Kosior et al. [47,91] on the bouncing behaviour of bubbles when impacting solid surfaces and free surfaces. As can be seen the bouncing is very similar, but in the free surface case the bubble bursts to the atmosphere while in the solid surface case the bubble does not.

Experimentally, it thus appears that the nature of the surface (solid surface or free surface) has a negligible effect on the global bouncing behaviour of a bubble (at least for these bubbles). Using a force balance model, it was shown that, though the bouncing behaviour is almost identical, the deformation of the free surface plays an important role in the dynamics of the bubble bounce [72]. Bubble bouncing behaviour was also predicted using full numerical simulations of the Navier–Stokes equations [102] for a flat horizontal surface.

4.6. The first appearance of the dimple

In Klaseboer et al. [87], while investigating approaching drops at a constant velocity, it was noted that, if the approach velocity remains constant, the governing equations could be non-dimensionalised in such a way that no parameters remain. Thus a universally valid solution could be found. This formula predicted that a dimple first occurs at a film height $h_D = 0.4RCa^{1/2}$ with $Ca = \mu V_T/\sigma$. If we compare with Eqs. (48)–(50), the equations we are solving here are very similar (provided the disjoining pressure Π in Eq. (49) is zero), but two factors 1/2 appear in Eqs. (49) and (50). Also a factor 'c' appears in Eq. (48) accounting for the immobile ($c = 1$) or mobile ($c = 4$) character of the water–air interface. With some rescaling it can easily be shown that for our bouncing bubble problem the following equation could hold:

$$h_D = 0.4R\sqrt{\frac{2\mu V_T}{c\sigma}} = 0.4R\sqrt{\frac{2Ca}{c}} \tag{53}$$

The factor '2' under the square root sign appears due to the factor 1/2 mentioned above. The first appearance of the dimple according to this equation is shown in Fig. 26 for a variety of experimental data. Strictly speaking, Eq. (53) is only valid for cases where the approach velocity remains constant at V_T. Comparing the velocity and film height plots, we can see that this is actually no longer the case. Nevertheless, just prior to the formation of the film the velocity is still very close to V_T. This is probably the reason that Eq. (53) still works very well as a first approximation.

In the above discussion we have introduced the capillary number, but previously we mentioned that the dynamics of the bubble should be governed by the Reynolds and Weber number. These numbers are actually related to each other by $Ca = We/\mathrm{Re}$. A similar law as Eq. (53) is valid for drops impacting on solid surfaces [104,105].

5. Conclusions

In this review, the rise and bounce of bubbles have been investigated in light of new experimental advances that allowed precise measurements of the trajectory and film heights simultaneously. The proposed theory showed to be effective in capturing the physical features of the problem all the way down to the colloidal size. The problem was tackled from both a film drainage point of view and from a force balance point of view. The force balance–lubrication framework is capable of predicting

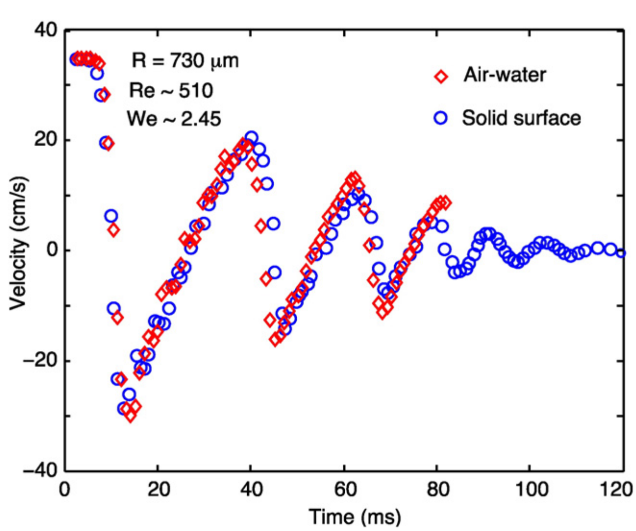

Fig. 25. Bounce of a bubble against solid surface vs bounce of a bubble against an air–water interface from Kosior et al. [47,91]. The amplitude of the bounce as well as period is very similar until eventually the bubble bursts at 90 ms.

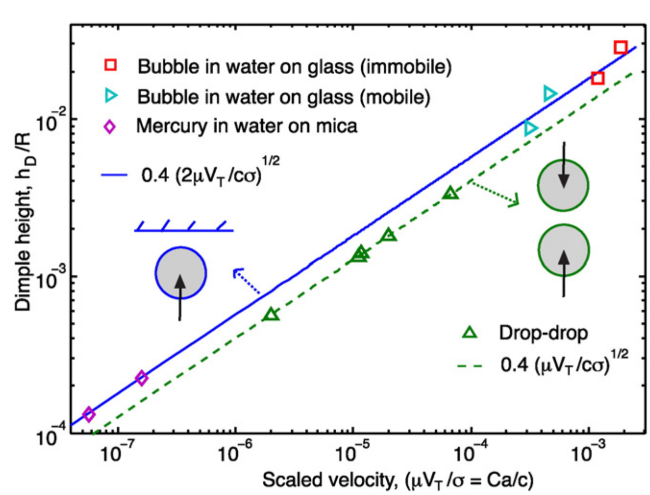

Fig. 26. Comparison of first appearance of dimple formation of Eq. (53) with different experimental systems from the literature: [9] (squares), [10] (blue triangles), [103] (diamonds) and [87] (green triangles).

the trajectory of the centre of mass and film evolution without any adjustable parameter. This is even feasible for bubbles with a high Reynolds number based on the approach velocity.

From a colloidal science point of view, for large bouncing bubbles, Van der Waals and electrical double layer forces can be neglected for the first few bounces, since the films that are being formed are always on the micrometre scale, while surface forces are typically only important if the film has thinned to the nanometre scale range or for very small bubbles. Surface mobility on the other hand can considerably change the dynamics of the bouncing bubble and/or its approach velocity. It is most likely that bubbles in real industrial systems, unless extreme care has been taken to eliminate impurities, will exhibit immobile rising behaviour and immobile film drainage. The rising velocity of a single bubble can confirm if the bubble rises under mobile or immobile conditions.

Though considerable progress using full numerical simulations involving multiphase systems has been achieved recently due to increase in computational power, it is still very challenging to use such techniques to capture the last stages of film drainage just before film rupture due to widely different length scales about one mm for the bubble radius, tens of micrometres for the film size and nanometres for the film height. The impact of bubbles on deformable surfaces adds one extra complication due two deforming surfaces that need to be tracked simultaneously and to high resolution and precision. This is a direction numerical simulations can develop. From the experimental point of view, being able to measure forces and film thickness simultaneously [106] for impacting bubbles at large approach speeds is still needed to further validate the theoretical results.

In many applications ranging from the bubbles stability and lifetimes in beverages to the aeration of bioreactors in which the dynamics of the interaction of bubbles with deformable interfaces is more pertinent, there is little detailed quantitative experimental data in this regard. Although the present theoretical framework can be extended to analyse the bubble interaction with deformable surfaces, the special case in which both interfaces have mobile (zero tangential stress) boundary conditions still requires the development of an accurate quantitative theoretical framework. Therefore, there remain experimental and theoretical challenges in the broad area of bubble interaction with soft interfaces.

Acknowledgements

We would like to thank Maurice Hendrix and Claus-Dieter Ohl for providing experimental data of bouncing bubbles. We thank Luke Parkinson and John Ralston for providing data on settling bubbles at low Reynolds numbers and Marta Krasowska and Kazimierz Malysa for providing movies on bouncing bubbles in clean conditions. DYCC is an Adjunct Professor at the National University of Singapore and gratefully acknowledges the financial support by the Australian Research Council through the Discovery Projects schemes (DP140100558).

References

[1] Prosperetti A. Phys Fluids 2004;16:1852.
[2] Ohl CD, Tijink A, Prosperetti A. J Fluid Mech 2003;482:271.
[3] Van Leeuwenhoek A, Alle de Brieven. In: Heniger J, editor. Deel, Vol. 9. Amsterdam: N.V. Swets & Zeitlinger; 1976. p. 1692–4.
[4] Young T. Philos Trans R Soc Lond 1805;95:65.
[5] Laplace P-S. Mécanique célesteSupplement to the tenth ed. ; 1806 412.
[6] Gauss CF. Principia generalia theoriae figurae fluidorum in statu aequilibrii. Göttingen: Dieterichs; 1830.
[7] Reynolds O. Philos Trans R Soc Lond 1886;177:157 [See also reprint in Reynolds O. Papers on mechanical and physical subjects, 1901, Vol II, Cambridge University Press].
[8] Derjaguin BV, Kussakov M. Acta Physicochim URSS 1939;10:25 [Reprinted in Prog Surface Sci 1992;40:26].
[9] Hendrix MHW, Manica R, Klaseboer E, Chan DYC, Ohl C-D. Phys Rev Lett 2012;108:247803.
[10] Manica R, Hendrix MHW, Gupta R, Klaseboer E, Ohl C-D, Chan DYC. Soft Matter 2013;9:9755.
[11] Mudde RF. Annu Rev Fluid Mech 2005;37:393.
[12] Hadamard JS. C R Acad Sci 1911;152:1735.
[13] Rybczynski W. Bull Acad Sci Cracow Ser A 1911;40.
[14] Kelsall GH, Tang S, Smith AL, Yurdakul S. Faraday Trans 1996;92:3879.
[15] Parkinson L, Sedev R, Fornasiero D, Ralston J. J Colloid Interface Sci 2008;322:168.
[16] Stokes GG. Camb Philos Trans 1851;9:8.
[17] Clift R, Grace JR, Weber ME. Bubbles, drops and particles. Academic Press; 1978.
[18] Magnaudet J, Eames I. Annu Rev Fluid Mech 2000;32:659.
[19] De Vries AWG, Biesheuvel A, van Wijngaarden L. Int J Multiphase Flow 2002;28:1823.
[20] Tomiyama A, Celata GP, Hosokawa S, Yoshida S. Int J Multiphase Flow 2002;28:1497.
[21] Wu M, Gharib M. Phys Fluids 2002;14:49.
[22] Maldonado M, Quinn JJ, Gomez CO, Finch JA. Chem Eng Sci 2013;98:7.
[23] Bhaga D, Weber ME. J Fluid Mech 1981;105:61.
[24] Bel Fdhila R, Duineveld PC. Phys Fluids 1996;8:310.
[25] Malysa K, Krasowska M, Krzan M. Adv Colloid Interface Sci 2005;114–115:205.
[26] Frumkin AN, Levich VG. Zh Phys Chim 1947;21:1183.
[27] Levich VG. Physicochemical hydrodynamics. Englewood Cliffs, NJ: Prentice-Hall; 1962.
[28] Harper JF. Adv Appl Mech 1972;12:59.
[29] Harper JF. J Fluid Mech 2004;521:115.
[30] Harper JF. J Fluid Mech 2007;581:157.
[31] Cuenot B, Magnaudet J, Spennato B. J Fluid Mech 1997;339:25.
[32] Palaparthi R, Papageorgiou DT, Maldarelli C. J Fluid Mech 2006;559:1.
[33] Sadhal S, Johnson R. J Fluid Mech 1983;126:237.
[34] Brenner H. Chem Eng Sci 1961;16:242.
[35] Bart E. Chem Eng Sci 1968;23:193.
[36] Parkinson L, Ralston J. J Phys Chem C 2010;114:2273.
[37] Manica R, Parkinson L, Ralston J, Chan DYC. J Phys Chem C 2010;114:1942.
[38] Parkinson L, Ralston J. Adv Colloid Interface Sci 2011;168:198.
[39] Tsao H-K, Koch DL. Phys Fluids 1997;9:44.
[40] Jachimska B, Warszynski P, Malysa K. Colloids Surf A Physicochem Eng Asp 1998;143:429.
[41] Jachimska B, Warszynski P, Malysa K. Progr Colloid Polym Sci 2000;116:120.
[42] Zawala J, Krasowska M, Dabros T, Malysa K. Can J Chem Eng 2007;85:669.
[43] Zenit R, Legendre D. Phys Fluids 2009;21:083306.
[44] Suñol F, González-Cinca R. Colloids Surf A Physicochem Eng Asp 2010;365:36.
[45] Zawala J, Malysa K. Langmuir 2011;27:2250.
[46] Zawala J, Dorbolo S, Terwagne D, Vandewalle N, Malysa K. Soft Matter 2011;7:6719.
[47] Kosior D, Zawala J, Krasowska M, Malysa K. Phys Chem Chem Phys 2013;15:2586.
[48] Fisher LR, Mitchell EE, Hewitt D, Ralston J, Wolfe J. Colloids Surf 1991;52:163.
[49] Fisher LR, Hewitt D, Mitchell EE, Ralston J, Wolfe J. Adv Colloid Interface Sci 1992;39:397.
[50] Manica R, Chan DYC. Phys Chem Chem Phys 2011;13:1434.
[51] Manica R, Hendrix MHW, Klaseboer E, Ohl C-D, Chan DYC. Appl Math Model 2014;38:4249.
[52] Donoghue DB, Albadawi A, Delauré YMC, Robinson AJ, Murray DB. Int J Heat Mass Transf 2014;71:439.
[53] Batchelor GK. An introduction to fluid dynamics. Cambridge University Press; 1967.
[54] Ryskin G, Leal LG. J Fluid Mech 1984;148:19.
[55] Yang B, Prosperetti A, Takagi S. Phys Fluids 2003;15:2640.
[56] Scardovelli R, Zaleski S. Annu Rev Fluid Mech 1999;31:567.
[57] Pozrikidis C. Introduction to theoretical and computational fluid dynamics. 2nd ed. Oxford University Press; 2011.
[58] Basset AB. A treatise on hydrodynamics, vol. II. Deighton: Bell and Sons; 1888[Chapter XXII].
[59] Yang S, Leal LG. Phys Fluids 1822;A1991:3.
[60] Zapryanov Z, Tabakova S. Dynamics of bubbles, drops and rigid particles. Springer; 1999.
[61] Kamran K, Carnie SL. Chem Eng Sci 2013;104:361.
[62] Verwey EJW, Overbeek JTG. Theory of the stability of lyophobic colloids. Elsevier; 1948.
[63] Butt HJ, Graf K, Kappl M. Physics and chemistry of interfaces. Wiley-VCH; 2003.
[64] Derjaguin B. Kolloid Z 1939;69:155.
[65] Hunter RJ. Foundations of colloid science, vol. 1. Oxford: Clarendon Press; 1986.
[66] Klaseboer E, Manica R, Chan DYC, Khoo BC. Eng Anal Boundary Elem 2011;35:489.
[67] Lamb H. Hydrodynamics. Cambridge University Press; 1932.
[68] d'Alembert. Essai d'une nouvelle théorie de la résistance des fluides, Paris; 1752.
[69] Moore DW. J Fluid Mech 1965;23:749.
[70] Klaseboer E, Chevaillier J-P, Maté A, Masbernat O, Gourdon C. Phys Fluids 2001;13:45.
[71] Legendre D, Zenit R, Velez-Cordero JR. Phys Fluids 2012;24:043303.
[72] Manica R, Klaseboer E, Chan DYC. Soft Matter 2016;12:3271.
[73] Schiller L, Naumann A. Zeit Ver Deut Ing 1933;77:318.
[74] Duineveld PC. Bouncing and coalescence of two bubbles in water. [Ph.D Thesis] Twente University; 1994.
[75] Duineveld PC. J Fluid Mech 1995;292:325.
[76] Okazaki S. Bull Chem Soc Jpn 1964;37:144.
[77] Raymond F, Rosant J-M. Chem Eng Sci 2000;55:943.
[78] Cano-Lozano JC, Bohorquez P, Martínez-Bazán C. Int J Multiphase Flow 2013;51:11.
[79] Magnaudet J, Mougin G. Phys Rev Lett 2001;88:014502.
[80] Magnaudet J, Mougin G. J Fluid Mech 2007;572:311.
[81] Miloh T. J Eng Math 1977;11:349.
[82] Kharlamov AA, Chara Z, Vlasak P. J Eng Math 2007;62:161.

[83] Yiantsios SG, Davis RH. J Fluid Mech 1990;217:547.
[84] Chan DYC, Klaseboer E, Manica R. Soft Matter 2011;7:2235.
[85] Chan DYC, Klaseboer E, Manica R. Soft Matter 2010;6:1809.
[86] Chan DYC, Klaseboer E, Manica R. Adv Colloid Interface Sci 2011;165:70.
[87] Klaseboer E, Chevaillier J-P, Gourdon C, Masbernat O. J Colloid Interface Sci 2000;229:274.
[88] Born M, Wolf E. Principles of optics: electromagnetic theory of propagation, interference and diffraction of light. 6th ed. Cambridge, U.K.: Cambridge University Press; 1997
[89] Moes H. J Magn Magn Mater 1991;95:1.
[90] Klaseboer E, Manica R, Hendrix MHW, Ohl C-D, Chan DYC. Phys Fluids 2014;26:092101.
[91] Kosior D, Zawala J, Krasowska M, Malysa K. Colloids Surf A Physicochem Eng Asp 2014;441:788.
[92] Manica R, Klaseboer E, Chan DYC. Langmuir 2015;31:6763.
[93] Bretherton FP. J Fluid Mech 1961;10:166.
[94] Klaseboer E, Gupta R, Manica R. Phys Fluids 2014;26:032107.
[95] Cherukumudi A, Klaseboer E, Khan SA, Manica R. Microfluid Nanofluid 2015;19:1221.
[96] Vakarelski IU, Manica R, Tang X, O'Shea SJ, Stevens GW, Grieser F, et al. PNAS 2010;107:11177.
[97] Yoon Y, Baldessari F, Ceniceros HC, Leal LG. Phys Fluids 2007;19:102102.
[98] Bremond N, Thiam AR, Bibette J. Phys Rev Lett 2008;100:024501.
[99] Guido S, Simeone M. J Fluid Mech 1998;357:1.
[100] Lai A, Bremond N, Stone HA. J Fluid Mech 2009;632:97.
[101] Chan DYC, Klaseboer E, Manica R. Soft Matter 2009;5:2858.
[102] Albadawi A, Donoghue DB, Robinson AJ, Murray DB, Delauré YMC. Int J Multiphase Flow 2014;65:82.
[103] Connor JN, Horn RG. Faraday Discuss 2003;123:193.
[104] Klaseboer E, Manica R, Chan DYC. Phys Rev Lett 2014;113:194501.
[105] Bouwhuis W, van der Veen RCA, Tran T, Keij DL, Winkels KG, Peters IR, et al. Phys Rev Lett 2012;109:264501.
[106] Shahalami M, Wang L, Wu C, Masliyah JH, Xu Z, Chan DYC. Adv Colloid Interface Sci 2015;217:31.